

See discussions, stats, and author profiles for this publication at:
<https://www.researchgate.net/publication/48879555>

Potential energy surfaces of ozone in its ground state and in the lowest-lying eight excited states

ARTICLE *in* CHEMICAL PHYSICS · DECEMBER 1993

Impact Factor: 1.65 · DOI: 10.1016/0301-0104(93)85059-H · Source: OAI

CITATIONS

94

READS

32

3 AUTHORS, INCLUDING:



[Sigrid D Peyerimhoff](#)

University of Bonn

488 PUBLICATIONS 16,013 CITATIONS

SEE PROFILE



[F. Grein](#)

University of New Brunswick

245 PUBLICATIONS 3,154 CITATIONS

SEE PROFILE

Potential energy surfaces of ozone in its ground state and in the lowest-lying eight excited states

Antonio Banichevich, Sigrid D. Peyerimhoff

Institut für Physikalische und Theoretische Chemie, Universität Bonn, Wegelerstrasse 12, 53115 Bonn, Germany

and

Friedrich Grein

University of New Brunswick, Department of Chemistry, Fredericton, New Brunswick, Canada E3B 6E2

Received 21 May 1993

Potential energy surfaces of the ground state and the lowest eight excited states of ozone which correlate with the three fragmentation limits $O(^3P_g) + O_2(X^3\Sigma_g^-)$, $O(^3P_g) + O_2(a^1\Delta_g)$ and $O(^1D_g) + O_2(a^1\Delta_g)$ are calculated employing multireference configuration interaction (MRD-CI) treatments in a Gaussian AO basis. Vertical and adiabatic transition energies as well as dissociation energies based on the optimized energy surface are presented. The transition moments between the ground state and the excited singlet states are also computed as a function of geometry and are employed to simulate Wulf, Chappuis and Huggins absorption bands. Some aspects about ozone predissociation and photodissociation and its formation are discussed.

1. Introduction

Although atmospheric ozone is a strong absorber of solar radiation in the visible and ultraviolet wavelengths, it is its photodissociative nature which influences the temperature structure in the stratosphere [1,2], where a sensitive interrelation between ozone concentration, chemistry, radiation field and dynamical processes is present [3].

The first four absorption bands of ozone have been studied for more than sixty years [4–7]. Later on absorption cross section measurements [8–10] have indicated that these bands possess very diffuse nature. This absorption behavior is shown in fig. 1 and some characteristics of each band are summarized in table 1. Generally it can be seen that two bell-shaped continua exist, one extending in the visible absorption range from 410 to 663 nm (≈ 15080 to 23260 cm^{-1}), and the second one extending in the ultraviolet absorption range from about 205 to 300 nm (33300 to 48800 cm^{-1}). Their maxima are between 597.5 and 602.5 nm [7,16,19] and around 250 nm, respectively.

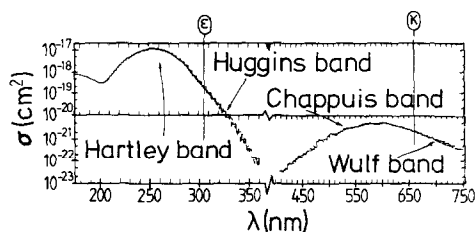


Fig. 1. Absorption cross sections for ozone as a function of incident wavelength from $\lambda = 180$ nm to the Wulf band adapted from ref. [11]. κ and ϵ denote the limits considered for the vibrational structure of the corresponding Wulf and Huggins bands, respectively.

The absorption band in the visible is known as the Chappuis band [6] and consists of a continuum plus a series of peaks superimposed on the blue side of the spectrum. Its band origin is found between 15750 and 16600 cm^{-1} [16,17]. The observed vibronic fine structure is described by progressions in ν_1 , ν_2 , whereby $\nu_3 = 0$ [16,17]. The absorption cross sections are found to be almost independent of the temperature [3,19].

Table 1
Characteristic features of the ozone bands for wavelengths $1000 \geq \lambda \geq 220$ nm

| Absorption band | Spectral region λ (nm) | Absorption ^{a)} cross section $\sigma(\lambda)$ (cm ²) | Peak ^{a)} (maximum) absorption $\sigma(\lambda)$ (cm ²) |
|-----------------|--------------------------------|--|--|
| Wulf | 663–1000 | $\sigma(663) = 1.85 \times 10^{-21}$ $\sigma(847.5\text{--}852.5) = 1.40 \times 10^{-22}$ | $\sigma(662.5) = 1.85 \times 10^{-21}$ |
| Chappuis | 410–663 | $\sigma(407.5\text{--}412.5) = 2.91 \times 10^{-23}$ $\sigma(663) = 1.85 \times 10^{-21}$ | $\sigma(597.5\text{--}602.5) = 4.89 \times 10^{-21}$ |
| Huggins | 312–352 | $\sigma(312.7\text{--}412.5) = 2.49 \times 10^{-20}\text{--}2.90 \times 10^{-23}$ | $\sigma(312.2\text{--}317.5) = 2.49 \times 10^{-20}$ |
| Hartley | 290–300 | $\sigma(290\text{--}303) = 1.09 \times 10^{-18}\text{--}1.85 \times 10^{-19}$ | – |
| | 270–238 | $\sigma(270\text{--}238) = 6.92 \times 10^{-18}\text{--}7.97 \times 10^{-18}$ | $\sigma(253\text{--}256) = 1.15 \times 10^{-17}$ |

^{a)} Data at $T=203$ K.

The absorption band in the ultraviolet range is known as the Hartley band [4] and consists of a very broad continuum plus a series of very narrow peaks superimposed near the maximum on both sides ($270 \leq \lambda \leq 238$ nm) [9,10,23,26]. The estimated band spacing for these series is between 200 and 300 cm^{-1} [23]. Its band origin is not known. At the maximum of this band ($\lambda=254$ nm) minimal temperature dependence (0.5%–1.0%) [10,25] has been found. For lower energies than $h\nu \leq 34500$ cm^{-1} ($\lambda \geq 290$ nm) an important temperature dependence exists [10,18].

On the red side of both previously discussed bell-shaped continua “falloff” regions characterized by peaks with very diffuse nature have been observed [9,10,12,16,22].

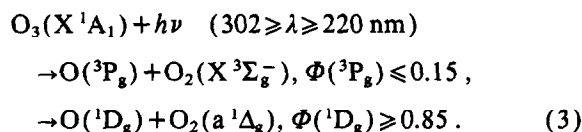
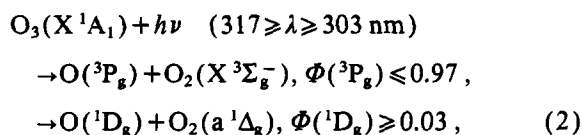
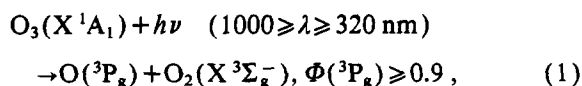
In the near-infrared wavelength region the first “falloff” region is known as the Wulf absorption band (the upper limit denoted in fig. 1 as κ). It consists of a series of peaks superimposed on the continuum of the visible range and possesses a band spacing between 530 and 568 cm^{-1} [7,12,13]; its band origin is around 10000 cm^{-1} [7,12]. The intensity of the observed peaks increases rapidly with excitation energy, but their corresponding width suggests that the lifetime of the peaks likewise decreases with excitation energy. The observed absorption cross sections for the measured lower limit of the “falloff” region at the wavelength range 847.5–852.5 nm (11732–11800 cm^{-1}) [3] give a value of $\sigma = 1.4 \times 10^{-22}$ cm^2 .

The second “falloff” region corresponding to the red side of the Hartley continuum is known as the Huggins band [5]. This absorption band is positioned in the ultraviolet A and B wavelength range extending from about 352 nm to about 312 nm (28400–32000 cm^{-1}) [9,10,20,21,23]. At the temperature $T=203$ K, the measured absorption cross section for the upper limit at 308 nm (32520 cm^{-1}) is about $\sigma = 4.33 \times 10^{-20}$ cm^2 [3]. The lower limit is found at $\lambda = [342.5\text{--}412.5]$ nm (24250–29200 cm^{-1}) with a measured value of $\sigma = 2.90 \times 10^{-23}$ cm^2 [3] ($T=203$ K). In this absorption region the end of the Chappuis band should also be expected and due to the low absorption cross sections this region can be interpreted as a window for ozone absorption.

Just as the Wulf band the Huggins band consists of a series of peaks superimposed on the continuum of the ultraviolet range. These series of peaks have been assigned in two different manners for which the most probable is $(\nu_1, \nu_2, \nu_3)' \leftarrow (000)''$ for $\nu_1' = 0\text{--}6$, $\nu_2' = 0$, 1 and $\nu_3' = 0\text{--}2$ [9,20–22]. The intensity of the observed progressions [9] increases rapidly with photoexcitation energy. The bands with wavelengths less than approximately 313.5 nm (31900 cm^{-1}) have irregular energy spacings which are probably caused by a perturbation. These irregularly spaced bands are in the region of the $\text{O}_2(a^1\Delta_g) + \text{O}(^1D_g)$ dissociation limit. An important temperature dependence in the absorption cross sections has been observed for this band [9,10,23,26].

| Temperature dependence | Characteristics of the band | Expectation from diffuse nature | Observed spacing in the progression (cm^{-1}) | Ref. |
|------------------------|-----------------------------|---------------------------------------|---|--------------------|
| expected | falloff region to the red | predissociative | $\delta\nu_1 \approx 1200$ $\delta\nu_2 \approx 560$ | [3,7,12–15] |
| minimal | bell-shaped continuum | predissociative and photodissociative | $\delta\nu_1 \approx 930\text{--}1200$ $\delta\nu_2 \approx 460\text{--}640$ | [3,7,14–19] |
| important | falloff region to the red | predissociative | $\delta\nu_1 \approx 628\text{--}707$ $\delta\nu_2 \approx 348\text{--}370$ $\delta\nu_3 \approx 738\text{--}778$ | [3,9,10,18,20–23] |
| important | falloff region to the red | predissociative and photodissociative | $\delta\nu_2 \approx 300$ | [5,10,18,20,23–26] |
| minimal | bell-shaped continuum | photodissociative | | [5,23,25,27–30] |

If one takes the experimental photofragmentation data [27–31] for absorbing ozone into account, the fragmentation based on the measured quantum yield $\Phi(\lambda)$, can be assumed to occur in the following reactions:



Photoprocess (1) can occur in the energy range of the Wulf, Chappuis and Huggins absorption bands; photoprocess (3) at $\lambda \leq 302 \text{ nm}$ is in the energy range of the Hartley band. Experimental studies found that the primary fragmentation due to these photoprocesses [28–31] is largely vibrationally adiabatic but rotationally impulsive, i.e. most of the available energy appears as fragment translation (> 50%). The photofragmentation process (2) beyond the nominal thermodynamic threshold of the singlet dissociation channel $\text{O}(^1\text{D}_g) + \text{O}_2(\text{a } ^1\Delta_g)$ at 303 nm has also been

observed [28–30,32] but a definitive interpretation is still lacking.

From the theoretical point of view several ab initio highly correlated techniques, such as the “perfect pairing” generalized valence bond (GVB-PP) multi-configuration SCF technique [33], many-body perturbation theory (MBPT) [34], singles and doubles coupled-cluster (CCSD and CCSDCT) method [35], CASSCF [36,37] and others [38–40] have been used in the last ten years for the study of this molecule. Many of them are restricted to the study of the potential energy surface (PES) of the electronic ground state; diabatic $^1\text{A}'$ excited states have almost exclusively been calculated [33,37].

In an effort to obtain not only a good description of the Franck–Condon region of this molecule but also of its photodissociation behavior, we have pursued a theoretical study for the ground and lowest eight electronic states (vertical excitation below 180 nm or 6.8 eV) in asymmetric nuclear arrangements, i.e. C_s symmetry. Singlet and triplet states are considered. The multireference configuration interaction (MRD-CI) treatment [41] is employed thereby. Three-dimensional potential energy surfaces (3D-PES) are generated in this study.

Section 2 presents technical details and discusses some aspects of the correlation between the electronic states and the dissociation limit. Section 3 treats the characterization of the singlet states as obtained from the 3D-PES. Section 4 presents the sim-

ulated absorption lines in the energy range of the Wulf, Chappuis and Huggins bands. Section 5 treats the characterization of the triplet states as obtained from the 2D-PES. Sections 6 and 7 discuss the *ab initio* results for the singlet and the triplet states and the final section contains a brief summary and the conclusions.

2. Technical details for the potential surface calculations

The oxygen functions are taken from the Dunning (9s, 5p) basis set in the [5s, 3p] contraction [42]. In addition one diffuse s, one diffuse p and one d polarization function was added so that the basis can be described as a contracted [6s, 4p, 1d] set. In addition one s-type Gaussian with exponent $\alpha = 1.15$ [43] was located between each pair of the oxygen atoms, so that the total AO basis employed in C_s symmetry consists of 75 contracted Cartesian Gaussians. The molecule is placed in the yz plane.

Considering asymmetrical deformation of the equilibrium geometry, the electronic configuration of the ozone ground state in C_s symmetry is

$$\dots (7a')^2 (8a')^2 (1a'')^2 (9a')^2 (10a')^2 (2a'')^2. \quad (4)$$

The SCF energy at equilibrium geometry is $E_{\text{SCF}} = -224.31893$ hartree.

For the CI calculations the SCF-MO of the lowest $^5A'$ state corresponding to the configuration

$$\dots (8a')^2 (9a')^2 (10a')^1 (11a')^1 (1a'')^2 (2a'')^1 (3a'')^1 \quad (5)$$

were chosen. This choice has the following advantages: at the fragmentation limit $O + O_2$ the various MO are characterized as $(8a', 1a'') \rightarrow (1\pi_{uy}, 1\pi_{ux})$, $9a' \rightarrow 2p_z$, $(10a', 2a'') \rightarrow (2p_y, 2p_x)$ and $(11a', 3a'') \rightarrow (1\pi_{vy}, 1\pi_{vx})$, so that $^5A'$ with the above occupation dissociates already at the SCF level of treatment into $O(1s^2 2s^2 2p_{x,y,z}^4)$ and $O_2(KK2\sigma_g^2 2\sigma_u^2 3\sigma_g^2 1\pi_u^4 1\pi_g^2)$. At the same time both degenerate components π_{gx} and π_{gy} of the O_2 molecule as well as the p_x and p_y AOs of the oxygen atom are equivalent in the SCF treatment. The $^5A'$ state is repulsive towards $O + O_2$ fragmentation.

The CI technique used is the multireference single- and double-excitation method (MRD-CI) employing configuration selection and energy extrapolation [41]. For the CI calculations in C_s symmetry 18 elec-

Table 2

Technical details of the MRD-CI calculations undertaken at the fixed geometry parameters $\gamma = 116.8^\circ$ and $R_1 = 2.413 a_0$ ^{a)}

| States treated ^{b)} | Number of reference configurations | Number of roots | Number of total SAF | Number of selected SAF | | $O_2 + O$ dissociation limit ^{c)} |
|---|------------------------------------|-----------------|---------------------|------------------------|------------------|---|
| | | | | $R_2 = 2.413 a_0$ | $R_2 = 10.0 a_0$ | |
| \tilde{X}^1A' (X^1A_1) \tilde{C}^1A' (A^1A') \tilde{D}^1A' (B^1A') \tilde{R}^1A' (R^1A') | 48 | 4 | 7180526 | 16034 | 13719 | I: $O(^3P_g) + O_2(X^3\Sigma_g^-)$ V: $O(^1D_g) + O_2(a^1\Delta_g)$ |
| \tilde{A}^1A'' (C^1A'') \tilde{B}^1A'' (D^1A'') \tilde{E}^1A'' (E^1A'') | 44 | 3 | 7292251 | 12826 | 13743 | I: $O(^3P_g) + O_2(X^3\Sigma_g^-)$ V: $O(^1D_g) + O_2(a^1\Delta_g)$ |
| \tilde{a}^3A' , \tilde{d}^3A' \tilde{r}^3A' , \tilde{s}^3A' | 41 | 4 | 13040967 | 15704 | 10203 | I: $O(^3P_g) + O_2(X^3\Sigma_g^-)$ II: $O(^3P_g) + O_2(a^1\Delta_g)$ |
| \tilde{b}^3A'' , \tilde{c}^3A'' \tilde{e}^3A'' , \tilde{f}^3A'' | 44 | 4 | 12961019 | 12284 | 13934 | I: $O(^3P_g) + O_2(X^3\Sigma_g^-)$ II: $O(^3P_g) + O_2(a^1\Delta_g)$ |

^{a)} Given are the number of reference (main) configurations and the number of roots according to which configuration selection is carried out, the total number of symmetry-adapted configuration state functions (SAF) which have been generated and the largest selected subspace which has been diagonalized explicitly. The weight of the reference configurations in the final MRD-CI wavefunction was larger than 89% for all states and internuclear separations R_1 . C_s subgroup irreducible representations are indicated in the first column.

^{b)} In parentheses the nomenclature used in previous work [44] is given.

^{c)} The calculated values for the dissociation limits can be found in refs. [44,45].

Because of the low dissociation energy ($D_e=1.13$ eV [24]) the asymmetric O+O₂ pathway has been considered to be the most likely pathway for fragmentation. The correlation diagrams between the C_{2v} symmetry in the Franck–Condon region and the C_s symmetry for asymmetric structures including the O₂+O dissociation are given in figs. 2 and 3 for sin-

In table 3 the calculated vertical excitation ener-

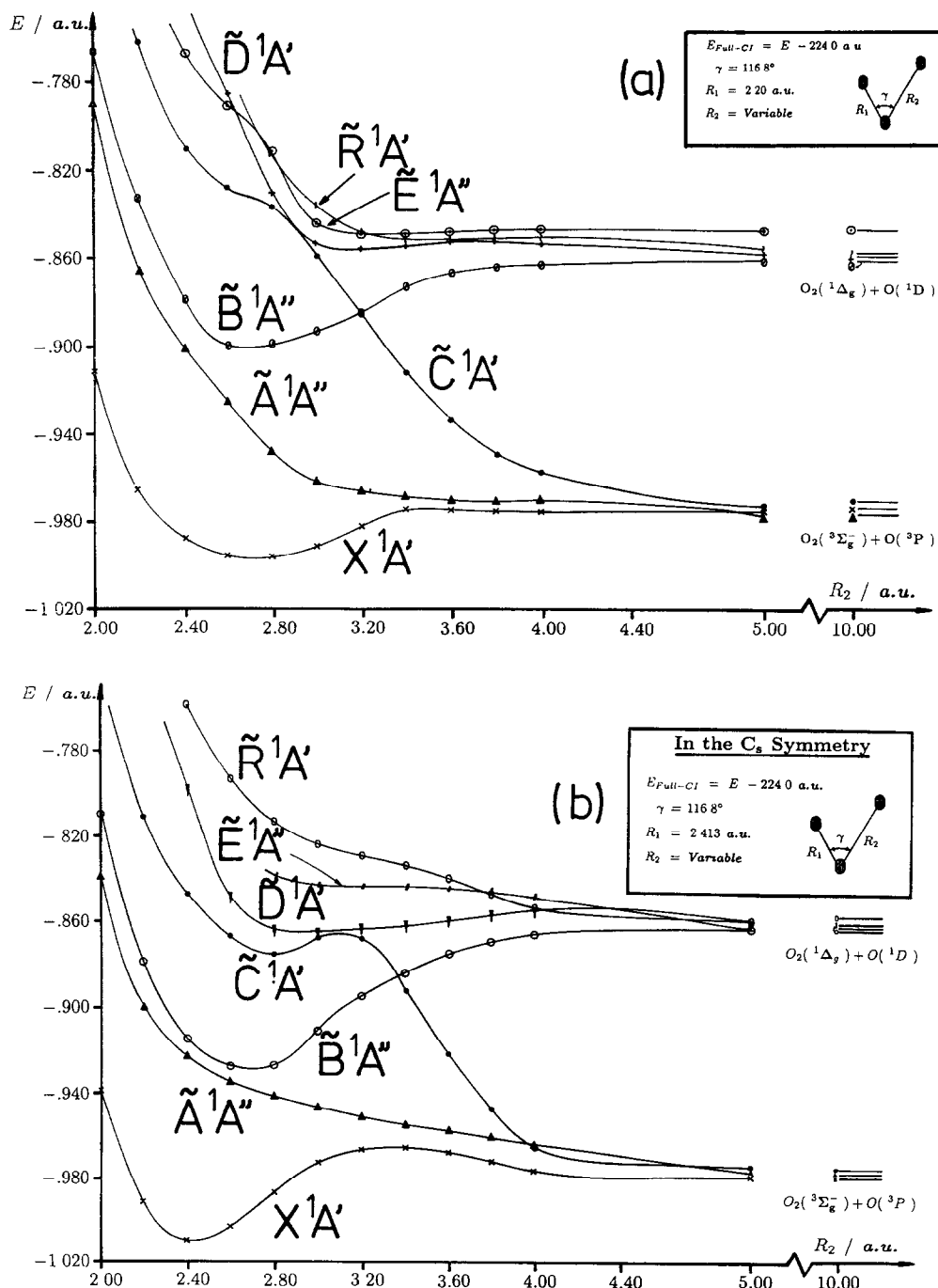


Fig. 4. Calculated potential energy curves for the lowest-lying singlet states of ozone as function of R_2 whereby the bond angle is held constant at 116.8° . (a) $R_1 = 2.20 a_0$, (b) $R_1 = 2.413 a_0$ and (c) $R_1 = 2.60 a_0$.

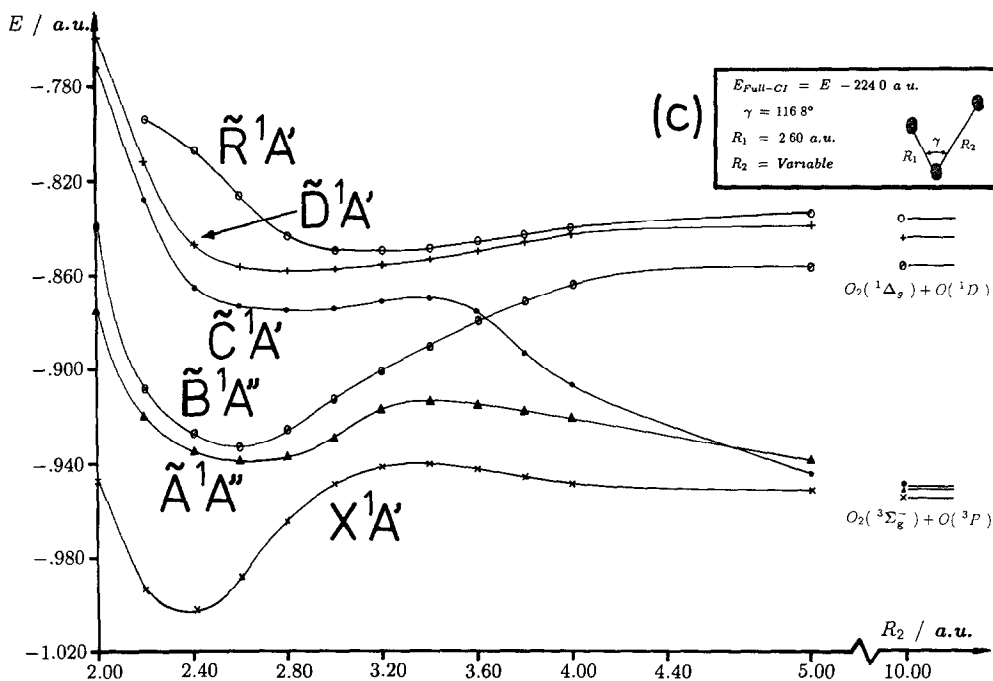


Fig. 4. Continued.

gies of the states treated formally in C_s symmetry are compared to the corresponding values obtained earlier for the symmetric C_{2v} nuclear arrangement [46]. Both sets of values are somewhat different. There are three technical reasons for this: (a) the AO basis sets in the C_{2v} and C_s calculations are slightly different, (b) the molecular orbitals employed in the MRD-CI treatment are the $^5A'$ MO (designed to describe dissociation properly) compared to natural orbitals in the C_{2v} treatment and (c) as a consequence the MRD-CI spaces also differ somewhat. Hence these deviations in the order of 0.2–0.3 eV should be considered as error margins.

3. Potential energy surfaces of the singlet states

For the calculation of the 3D-PES the set of grid points used was $2.0 a_0 \leq R_1 \leq 2.8 a_0$, $2.0 a_0 \leq R_2 \leq 10.0 a_0$ at three representative angles $\gamma = 100.0^\circ$, 116.8° and 133.2° . The lowest five electronic states have been treated in this entire range.

The estimated full-CI energy for the X^1A' ground state is $E_{\text{FCI}} = -225.01144$ hartree, obtained from the

calculation (see table 2) employing 48 reference configurations which lead to a total of 7180526 SAF and which are reduced to a selected subset of about 17000 in the Franck–Condon region.

The calculated potential curves for the variable R_2 at fixed geometrical values $R_1 = 2.20 a_0$, $2.413 a_0$ and $2.60 a_0$ at $\gamma = 116.8^\circ$, are shown in figs. 4a–4c, respectively. The character of the wavefunctions for the states considered is summarized in table 4 for various important internuclear separations R_2 ($R_1 = 2.413 a_0$ and $\gamma = 116.8^\circ$). Given are the dominant configurations in the wavefunction and the weight of all reference configurations. In table 5 the pertinent data of the states treated are summarized as obtained from the 3D-PES. Table 6 contains the calculated zero-point frequencies for the vibrational modes and table 7 the calculated spectroscopic parameters for the O_2 fragment in the O_3 supermolecule calculation, which indicates the level of accuracy achieved.

Table 4

Character of singlet electronic states. Given are the occupation numbers for the molecular orbitals in the dominant configurations at various internuclear separations R_2 for fixed geometry values ($R_1=2.413 a_0$; $\gamma=116.8^\circ$) and the weight K of all reference configurations ($K=\sum \text{ref } c_i^2$) in the CI expansion

| State | $R_2=2.413 a_0$ orbitals ^{a)} | | | | | | | | $R_2=3.00 a_0$ orbitals ^{a)} | | | | | | | | $R_2=4.00 a_0$ orbitals ^{a)} | | | | | | | |
|---------------------|---|-----|------|------|------|------|------|------|--|-----|------|------|------|------|------|------|--|-----|------|------|------|------|------|------|
| | 8a' | 9a' | 10a' | 11a' | 1a'' | 2a'' | 3a'' | K | 8a' | 9a' | 10a' | 11a' | 1a'' | 2a'' | 3a'' | K | 8a' | 9a' | 10a' | 11a' | 1a'' | 2a'' | 3a'' | K |
| X ¹ A' | 2 | 2 | 2 | 0 | 2 | 2 | 0 | 0.90 | 2 | 2 | 2 | 0 | 2 | 2 | 0 | 0.91 | – | – | – | – | – | – | – | 0.92 |
| | 2 | 2 | 2 | 0 | 2 | 0 | 2 | | 2 | 2 | 2 | 0 | 2 | 0 | 2 | | – | – | – | – | – | – | – | |
| | 2 | 2 | 2 | 0 | 2 | 1 | 1 | | 2 | 2 | 2 | 0 | 2 | 1 | 1 | | 2 | 2 | 2 | 0 | 2 | 1 | 1 | |
| | – | – | – | – | – | – | – | | – | – | – | – | – | – | – | | 2 | 2 | 0 | 2 | 2 | 1 | 1 | |
| Ã ¹ A'' | 2 | 2 | 1 | 0 | 2 | 2 | 1 | 0.90 | 2 | 2 | 1 | 0 | 2 | 2 | 1 | 0.91 | – | – | – | – | – | – | – | 0.92 |
| | 2 | 2 | 1 | 0 | 2 | 1 | 2 | | – | – | – | – | – | – | – | | – | – | – | – | – | – | – | |
| | – | – | – | – | – | – | – | | 2 | 1 | 2 | 0 | 2 | 2 | 1 | | 2 | 1 | 2 | 0 | 2 | 2 | 1 | |
| | 2 | 1 | 2 | 0 | 2 | 1 | 2 | | 2 | 1 | 2 | 0 | 2 | 1 | 2 | | – | – | – | – | – | – | – | |
| B̃ ¹ A'' | – | – | – | – | – | – | – | 0.90 | 2 | 2 | 1 | 0 | 2 | 2 | 1 | 0.91 | – | – | – | – | – | – | – | 0.92 |
| | 2 | 1 | 2 | 0 | 2 | 2 | 1 | | 2 | 1 | 2 | 0 | 2 | 2 | 1 | | 2 | 1 | 2 | 0 | 2 | 2 | 1 | |
| | 2 | 1 | 2 | 0 | 2 | 1 | 2 | | – | – | – | – | – | – | – | | – | – | – | – | – | – | – | |
| | – | – | – | – | – | – | – | | – | – | – | – | – | – | – | | 2 | 1 | 1 | 1 | 2 | 2 | 1 | c) |
| C̃ ¹ A' | 2 | 1 | 1 | 0 | 2 | 2 | 2 | 0.90 | 2 | 1 | 1 | 0 | 2 | 2 | 2 | 0.91 | – | – | – | – | – | – | – | 0.92 |
| | – | – | – | – | – | – | – | | 1 | 1 | 1 | 1 | 2 | 2 | 2 | | 1 | 1 | 2 | 2 | 2 | 1 | 2 | |
| | – | – | – | – | – | – | – | | – | – | – | – | – | – | – | | 2 | 1 | 2 | 1 | 2 | 1 | 1 | d) |
| | – | – | – | – | – | – | – | | – | – | – | – | – | – | – | | – | – | – | – | – | – | – | |
| D̃ ¹ A' | 2 | 2 | 2 | 0 | 2 | 0 | 2 | 0.90 | 2 | 2 | 2 | 0 | 2 | 0 | 2 | 0.90 | – | – | – | – | – | – | – | 0.92 |
| | 2 | 2 | 0 | 0 | 2 | 2 | 2 | | – | – | – | – | – | – | – | | – | – | – | – | – | – | – | |
| | – | – | – | – | – | – | – | | 2 | 2 | 1 | 1 | 2 | 0 | 2 | | – | – | – | – | – | – | – | |
| | – | – | – | – | – | – | – | | – | – | – | – | – | – | – | | 2 | 1 | 1 | 0 | 2 | 2 | 2 | |
| | 2 | 2 | 2 | 0 | 2 | 1 | 1 | | 2 | 2 | 2 | 0 | 2 | 1 | 1 | | – | – | – | – | – | – | – | |
| | – | – | – | – | – | – | – | | – | – | – | – | – | – | – | | 2 | 2 | 1 | 1 | 2 | 1 | 1 | b) |

^{a)} For the supermolecule calculation at $R_2=10.0 a_0$ the molecular orbitals describe the fragments $O(1s^2 2s^2 2p^4_{(x,y,z)})$, $O_2(...2\sigma_g^2 2\sigma_g^2 3\sigma_g^2 1\pi_{g(x,y)}^2 1\pi_{g(x,y)}^2)$ and $O_2(...2\sigma_g^2 2\sigma_g^2 3\sigma_g^2 1\pi_{u(x,y)}^2 1\pi_{u(x,y)}^2)$ with the following ordering: $2a'' \rightarrow 2p_x$, $9a' \rightarrow 2p_z$, $10a' \rightarrow 2p_y$, $7a' \rightarrow 3\sigma_g$, $1a'' \rightarrow 1\pi_{ux}$, $8a' \rightarrow 1\pi_{uy}$, $3a'' \rightarrow 1\pi_{gz}$, $11a' \rightarrow 1\pi_{gz}$.

^{b)} For this channel at $R_2=10.0 a_0$ the fragmentations $O(^3P_g) + O_2(X^3\Sigma_g^-)$ and $O(^1D_g) + O_2(a^1\Delta_g)$ are described by the configuration $...2p_x^1 2p_y^1 2p_z^1 ... 3\sigma_g^2 1\pi_u^4 1\pi_g^2$.

^{c)} For this channel at $R_2=10.0 a_0$ the fragmentations $O(^3P_g) + O_2(X^3\Sigma_g^-)$ and $O(^1D_g) + O_2(a^1\Delta_g)$ are described by the configuration $...2p_x^2 2p_y^1 2p_z^1 ... 3\sigma_g^2 1\pi_u^4 1\pi_g^2$.

^{d)} For this channel at $R_2=10.0 a_0$ the fragmentations $O(^3P_g) + O_2(X^3\Sigma_g^-)$ and $O(^1D_g) + O_2(a^1\Delta_g)$ are described by the configuration $...2p_x^1 2p_y^2 2p_z^1 ... 3\sigma_g^2 1\pi_u^4 1\pi_g^2$.

3.1. The ¹A' states

For the irreducible representation ¹A' four electronic states have been considered in analogy to previous diabatic treatments [33,37]. The 2D-PES corresponding to the stretching of both O–O bond lengths (R_1, R_2) for the X ¹A', C̃ ¹A' and D̃ ¹A' electronic states of ozone are presented in figs. 5a–5c, respec-

tively at the fixed angle 116.8° . They show the following characteristics:

(i) The ground state PES shows that the global minimum calculated at $R_1=R_2=2.41 a_0$ and $\gamma=116.6^\circ$ is separated from the dissociation region ($R_i \geq 4.0 a_0$, $i=1, 2$) by a potential barrier. The energy difference from minimum to the top of the barrier is calculated as $\Delta E=1.18 \text{ eV}$ (exp. $D_e=1.13 \text{ eV}$ [24]). Taking the energy difference between the

Table 5
Comparison of some theoretical and experimental spectroscopic parameters for the singlet states of O_3 . Distances in a_0 and energies in eV

| Electronic states in | | Excitation energy | | Optimized equilibrium geometry (R_1, R_2, γ) | | | Barriers and dissociation energy | | |
|----------------------|--|-------------------|-----------|---|----------------------|----------------------|-----------------------------------|-----------------------------------|--------------------|
| | | vertical | adiabatic | exp. ^{a)} | theory | exp. | theory ₁ ^{b)} | theory ₂ ^{c)} | exp. ^{d)} |
| C_{2v} | C_s | | | | | | | | |
| X^1A_1 | X^1A_1 | 0.0 | 0.0 | 0.0 | (2.41, 2.41, 116.6°) | (2.41, 2.41, 116.1°) | 1.18 | 0.91 | 1.13 |
| 1^1A_2 | $\left\{ \begin{array}{l} \tilde{A}^1A'' \\ \tilde{B}^1A'' \end{array} \right\}$ | 2.41 | 1.48 | 1.24–1.87 | (2.55, 2.55, 100.0°) | (2.55, 2.55, 101.5°) | 0.45 | – | – |
| | | 2.64 | 2.10 | 1.87–3.02 | (2.56, 2.56, 116.0°) | (2.57, 2.57, 116.2°) | 1.88 | 1.79 | – |
| 2^1A_1 | \tilde{C}^1A' | 4.38 | 3.55 | 3.03–3.80 | (2.65, 2.65, –) | – | 0.27 | – | – |
| 1^1B_2 | \tilde{D}^1A' | 5.47 | 3.86 | 3.53–5.80 | (2.44, 2.86, ~109°) | – | 0.44 | <0.10 | ~0.60 |

^{a)} The experimental limits for the absorption bands have been taken from the measured spectra. See refs. [7,9,10,12,13,16,18–23]. For the values given for the \tilde{C}^1A' state see text.

^{b)} The energy difference between the local minimum and the top of the barrier in direction to the dissociation limit is considered. In case of the \tilde{B}^1A' state the energy difference between $R_1 = R_2 = 2.56 a_0$ and $R_1 = 2.413 a_0$ and $R_2 = 10.0 a_0$ is given.

^{c)} For this value the energy difference between global minimum and the dissociation limit $O + O_2$ has been considered for the geometrical values $R_1 = \text{opt.}$ (describing the minimum of the diatomic), $R_2 = 10.0 a_0$ and $\gamma = 116.8^\circ$.

^{d)} The experimental value for the dissociation of the \tilde{D}^1A' state has been taken from refs. [20,22].

global minimum and the dissociation limit $O(^3P_g) + O_2(X^3\Sigma_g^-)$ the value is 0.91 eV. The wavefunction of this state is dominated between $R_2 = 2.0 a_0$ and $R_2 = 3.0 a_0$ (for $R_1 = 2.413 a_0$ and $\gamma = 116.8^\circ$) by the closed-shell configuration, $\hat{A} = \dots 8a'^2 9a'^2 10a'^2 1a''^2 2a''^2$ (see fig. 6). Between $R_2 = 3.0 a_0$ and $R_2 = 3.4 a_0$ a configuration interaction exists between configuration \hat{A} and the configuration $\hat{B}(10a' \rightarrow 11a')$ from which the barrier results. For $R_2 \geq 4.0 a_0$ the configuration with four open shells $\hat{C} = \dots 8a'^2 9a'^2 10a'^2 11a'^2 1a''^2 2a''^2 3a''^2$ becomes the leading term in the total range of the PES considered. The dissociation limit describes the $^3P_g(\dots 2p_x^1 2p_y^1 2p_z^1) + X^3\Sigma_g^-(\dots 1\pi_{ux}^2 1\pi_{uy}^2 1\pi_{gx}^1 1\pi_{gy}^1)$ fragmentation (see table 4). The zero-point frequencies are calculated as $\nu_1 = 1126 \text{ cm}^{-1}$, $\nu_2 = 740 \text{ cm}^{-1}$ and $\nu_3 = 1104 \text{ cm}^{-1}$ and show a very good agreement with the corresponding experimental data (see table 6).

(ii) The excited state, \tilde{C}^1A' , which dissociates in the lowest fragmentation channel $O(^3P_g) + O_2(X^3\Sigma_g^-)$, has a vertical energy of 4.38 eV. As shown in fig. 5b (at $\gamma = 116.8^\circ$) it possesses a small barrier which separates the global minimum (calculated at $R_1 = R_2 = 2.65 a_0$ with an adiabatic energy of 3.55 eV) from the dissociation limit (see also fig. 4c). From the angular variation it has been found that this state possesses a repulsive behavior at $\gamma = 116.8^\circ$ for the (R_1, R_2) PES in agreement with previous work [46]. The equilibrium angle for the expected two minima has not been investigated, but they are expected to be found for $\gamma \leq 100^\circ$ (global minimum) and for $\gamma = 125^\circ$. The calculated energy difference from the minimum at $\gamma = 116.8^\circ$ to the top of the barrier is 0.27 eV.

The wavefunction of this state at $\gamma = 116.8^\circ$ and $R_1 = 2.413 a_0$ is dominated between $R_2 = 2.0 a_0$ and $2.80 a_0$ (see table 4) by the two-open-shell configuration (double excitation $9a' 10a' \rightarrow 3a''^2$) $\hat{D} = \dots 8a'^2 9a'^1 10a'^1 1a''^2 2a''^2 3a''^2$. For $R > 3.0 a_0$ an interaction between the configurations \hat{D} , $\hat{E} = \dots 8a'^1 9a'^1 10a'^1 11a'^1 1a''^2 2a''^2 3a''^2$ and $\hat{F} = \dots 8a'^2 9a'^1 10a'^2 11a'^1 1a''^2 2a''^1 3a''^1$ exists from which the barrier results. For $R_2 > 4.0 a_0$ the wavefunction is characterized only by the four-open-shell configuration \hat{F} which at the dissociation limit ($R_2 = 10.0 a_0$) describes the $^3P_g(\dots 2p_x^1 2p_y^1 2p_z^1) + X^3\Sigma_g^-(\dots 1\pi_{ux}^2 1\pi_{uy}^2 1\pi_{gx}^1 1\pi_{gy}^1)$ fragmentation.

Table 6

Comparison of calculated and experimental zero-point frequencies in $^{16}\text{O}_3$. Also given is the transition energy from $(000)' \leftarrow (000)''$ with $\Delta E_0 = \Delta E - E_{(000)'} + E_{(000)'}$, for which ΔE is the adiabatic energy. All values are given in cm^{-1} (the standard notation is employed: prime for the excited state, double prime for the ground state)

| State | Present work | | | | Other theoretical works | | | Experiment | | | | |
|--------------------|--------------|---------|---------|-----------------|-------------------------|-------------------|--------------------|----------------|-------------------|-------------------|--------------|---------|
| | ν_1 | ν_2 | ν_3 | $\Delta E_0^a)$ | ν_1 | ν_2 | ν_3 | ν_1 | ν_2 | ν_3 | ΔE_0 | refs. |
| X^1A_1 | 1126 | 740 | 1104 | 1485 | 1134 | 713 | 1097 ^{b)} | 1110 | 705 | 1042 | 1429 | [24] |
| | | | | | 1173 | 737 | 1089 ^{c)} | 1103 | 701 | 1042 | 1423 | [47] |
| | | | | | — | — | — | 1135 | 716 | 1089 | 1470 | [48] |
| \tilde{A}^1A'' | 1170 | 573 | 996 | 12895 | 1183 | 598 | — ^{c)} | — | 566 | — ^{a)} | — | [7] |
| | | | | | — | — | — | — | 480 | — ^{a)} | — | [13] |
| | | | | | — | — | — | ≈ 1200 | 528 | — ^{a)} | 9544 | [12] |
| \tilde{B}^1A'' | 995 | 426 | 1024 | 16674 | 1171 | 619 | 904 ^{c)} | 930 | 460 | — ^{b)} | — | [17] |
| | | | | | — | — | — | ≈ 1210 | ≈ 640 | — ^{b)} | 15980 | [16] |
| $\tilde{C}^1A'^d)$ | 690 | 330 | 660 | 27990 | — | — | — | 636 | 352 | — ⁱ⁾ | — | [24] |
| | | | | | — | — | — | 628 | 348 ^{e)} | 738 ⁱ⁾ | 28447 | [21] |
| | | | | | — | — | — | 707 | 370 ^{e)} | 778 ⁱ⁾ | — | [20] |
| \tilde{D}^1A' | 770 | 612 | 586 | 30630 | 564 ^{f)} | 297 ^{f)} | 844 ^{f)} | — | ≈ 300 | — ^{j)} | — | [23,24] |

^{a)} For the ground state $\Delta E = E_{(000)'} = \frac{1}{2}(\nu_1 + \nu_2 + \nu_3)$. In case of \tilde{A}^1A'' state the considered transition is $(001)' \leftarrow (000)''$.

^{b)} Ref. [36]. ^{c)} Refs. [15,38].

^{d)} The calculated vibrational modes have been considered at the top of the barrier in the 3D-PES. See text.

^{e)} In the literature these values correspond to the constant $\nu_2 + X_{22}$ [20,21].

^{f)} Evaluated as the energy difference between the given position lines $[(200)' - (300)']$, $[(200)' - (210)']$ and $[(200)' - (201)']$ from ref. [49]. All theoretical values should be compared also to the experimental values for the Huggins band (see i)).

^{g)} Values given for the Wulf absorption band. ^{h)} Values given for the Chappuis absorption band.

ⁱ⁾ Values given for the Huggins absorption band. ^{j)} Value given for the Hartley absorption band.

The \tilde{C}^1A' state corresponds to the 2^1A_1 (C_{2v}) symmetry [46], and can be populated in the Franck-Condon region only by two-electron excitations, i.e. a zero-order forbidden transition. The calculated vibrational modes are listed in table 6. The bending mode has been evaluated for the vibrational levels in the repulsive part of the potential of this state in the Franck-Condon region. It should be pointed out that until today no definite interpretation exists for the observed line spacing in the Huggins band (fig. 1). We compare in table 6 our theoretical values for the \tilde{C}^1A' state to a band which could correspond to the $\tilde{D}^1A' \leftarrow X^1A'$ transition in the Huggins absorption range. In the next section we will present a simulated absorption pattern for the $\tilde{C}^1A' \leftarrow X^1A'$ transition and will discuss whether this transition really represents a transparent transition (too weak) compared to the \tilde{D}^1A' state.

(iii) The high-lying state, \tilde{D}^1A' , which dissociates into the excited fragments $\text{O}(^1D_g) + \text{O}_2(^1\Delta_g)$ has been calculated with a vertical energy of 5.47 eV. As shown in fig. 5c (at $\gamma = 116.8^\circ$) it possesses a mini-

mum in C_s geometry outside of the Franck-Condon region with $R_1 = 2.44 a_0$ and $R_2 = 2.86 a_0$. This minimum is at the adiabatic energy 3.86 eV above the ground state for an optimized angle of about 109° , i.e. it is below the dissociation limit by less than 0.10 eV and shows a barrier of 0.44 eV (see table 5).

The wavefunction of this state at $\gamma = 116.8^\circ$ and $R_1 = 2.413 a_0$ (see table 4) is described between $R = 2.0 a_0$ and $R \leq 3.2 a_0$ by the configurations with the single-excitation $\hat{G} = \dots 8a'^2 9a'^2 10a'^2 1a''^2 2a''^1 3a''^1$, and with the double-excitations $\hat{H} = \dots 8a'^2 9a'^2 10a'^2 1a''^2 2a''^0 3a''^2$ and $\hat{I} = \dots 8a'^2 9a'^2 10a'^0 1a''^2 2a''^2 3a''^2$. For $R > 3.2 a_0$ the wavefunction is dominated by the corresponding two-excitation configuration $\hat{D} = \dots 8a'^2 9a'^1 10a'^1 1a''^2 2a''^2 3a''^2$, which describes the \tilde{C}^1A' state in the Franck-Condon region, i.e. a non-adiabatic interaction occurs between the \tilde{C}^1A' and \tilde{D}^1A' states. The resulting avoided crossing between these states is quite obvious from figs. 4a–4c. For $R_2 \geq 4.0 a_0$ another configuration contributes with important coefficients. It is the four-open-

Table 7

Comparison of theoretical and experimental spectroscopic parameters for the O₂ fragment in the O₃ supermolecule calculation at $R_2 = 10.0 a_0$ and $\gamma = 116.8^\circ$. All values are given in cm⁻¹

| X ³ Σ _g ⁻ electronic state fragment | | | | |
|--|-------|------------|-------|--------------------|
| Dissociating state | R_e | ω_e | B_e | $T_e^{a,c)}$ |
| X ¹ A' | 2.30 | 1623 | 1.43 | 0.0 (-224.9782) |
| \tilde{A} ¹ A" | 2.39 | 1604 | 1.32 | 0.0 (-224.9788) |
| \tilde{C} ¹ A" | 2.36 | 1583 | 1.35 | 0.0 (-224.9761) |
| exp. ^{b)} | 2.28 | 1580 | 1.46 | 0.0 |

a ¹Δ_g electronic state fragment

| Dissociating state | R_e | ω_e | B_e | $T_e^{a)}$ |
|-----------------------------|-------|------------|-------|---------------------|
| \tilde{B} ¹ A" | 2.32 | 1501 | 1.39 | 8049 (-224.8687) |
| \tilde{D} ¹ A' | 2.30 | 1882 | 1.42 | 8146 (-224.8684) |
| exp. ^{d)} | 2.30 | 1510 | 1.42 | 7920 |

^{a)} In parentheses is given the calculated minimum energy (in hartree) for O₂ from the supermolecule calculation.

^{b)} Ref. [50].

^{c)} It represents the energy difference between the theoretical zero of energy $E_0 = -224.9777$ hartree averaged over all three singlet electronic states which dissociate into O₂(X ³Σ_g⁻) + O(³P_g) and the excited state a ¹Δ_g plus the experimental energy difference between the ³P_g and ¹D_g electronic states of the oxygen atom (15890 cm⁻¹).

^{d)} Ref. [51].

shell \tilde{C} previously discussed for the ground state. At the dissociation limit ($R_2 = 10.0 a_0$) it describes the ¹D_g(...2p_x¹2p_y¹2p_z²) + a ¹Δ_g(...1π_{ux}²1π_{uy}²1π_{gx}¹1π_{gy}¹) fragmentation.

The calculated vibrational frequencies $\nu_1 = 770$ cm⁻¹, $\nu_2 = 612$ cm⁻¹ and $\nu_3 = 586$ cm⁻¹ show important discrepancies compared to the values in another theoretical study [49] and also to the experimental values given for the Huggins absorption band (see table 6 and note i), if the latter absorption band is assigned by the \tilde{D} ¹A' ← X ¹A' transition.

(iv) The high-lying state, \tilde{R} ¹A' has not been investigated at the level of a 3D-PES. It has a vertical energy of 6.76 eV and it is correlated to the C_{2v} state

2 ¹B₂. It is a repulsive state which dissociates into O(¹D_g) + O₂(a ¹Δ_g) (see figs. 4a–4c).

In the Franck–Condon region the wavefunction of this state is dominated by the configurations $\hat{G} = \dots 8a'^2 9a'^2 10a'^2 1a''^2 2a''^1 3a''^1$ (one-electron excitation), $\hat{I} = \dots 8a'^2 9a'^2 10a'^0 1a''^2 2a''^2 3a''^2$ and $\hat{H} = \dots 8a'^2 9a'^2 10a'^2 1a''^2 2a''^0 3a''^2$ (two-electron excitations), i.e. it is described by the same configurations as the \tilde{D} ¹A' state. For $R_2 \geq 4.0 a_0$ the wavefunction is dominated by the configuration \hat{F} which has been described in the \tilde{C} ¹A' state. This four-open-shell configuration leads at the dissociation limit ($R_2 = 10.0 a_0$) to the ¹D_g(...2p_x¹2p_y²2p_z¹) + a ¹Δ_g(...1π_{ux}²1π_{uy}²1π_{gx}¹1π_{gy}¹) fragmentation.

3.2. The ¹A" states

The 2D-PES corresponding to the stretching of both O–O bonds (R_1, R_2) for the \tilde{A} ¹A" and \tilde{B} ¹A" electronic states of ozone are presented in fig. 7a, 7b and 7c, respectively. They show the following characteristics:

(i) The electronic state \tilde{A} ¹A" is the lowest excited singlet state in ozone. Its global minimum calculated at $R_1 = R_2 = 2.55 a_0$ and $\gamma = 100.0^\circ$ (fig. 7a) is separated from the dissociation region ($R_i \geq 3.5 a_0, i = 1, 2$) by a potential barrier. It is adiabatically 1.48 eV (table 5) above the ground state equilibrium. The energy difference between the ¹A" minimum and the top of its barrier has been calculated as $\Delta E = 0.45$ eV, i.e. 1.93 eV above the global minimum of the ground state. At the angle value $\gamma = 116.8^\circ$ (Franck–Condon region; see fig. 7b) this state is repulsive with a vertical excitation of 2.41 eV.

This state dissociates into the lowest fragmentation channel O(³P_g) + O₂(X ³Σ_g⁻). The barrier results from avoided crossings with the higher state \tilde{B} ¹A"; both correlate in C_{2v} symmetry with the 1 ¹A₂ and 1 ¹B₁ states (fig. 2) but possess the same A" symmetry in the distorted geometry and are thus allowed to interact [15,38,44]. As shown in fig. 8a, the PES of 1 ¹A₂ and 1 ¹B₁ states cross two times at $\gamma = 116^\circ$, when viewed as function of the $R_1 = R_2 = R$ bond distance elongation (see ref. [46]). One crossing is positioned in the Franck–Condon region around $R \approx 2.40 a_0$ and the second one at $R \geq 2.70 a_0$. Similar crossings have also been found in other triatomic systems such as H₂S [52], for example.

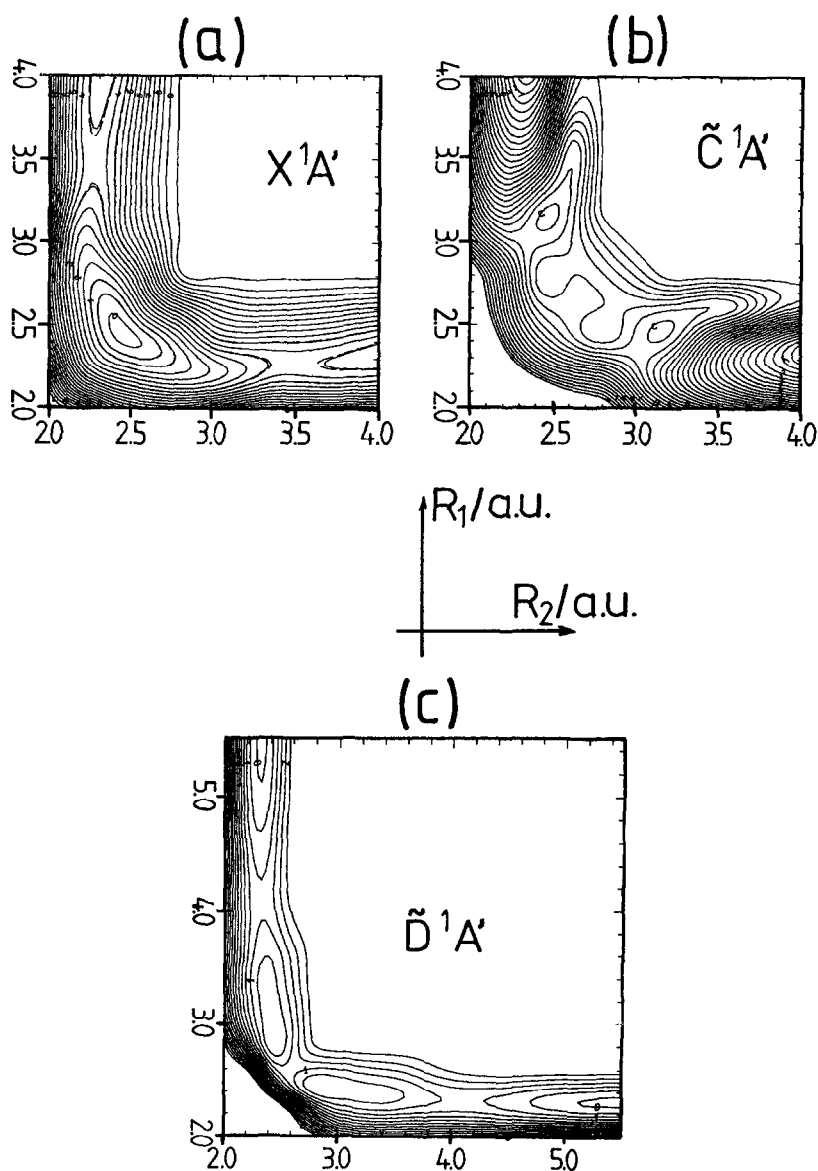


Fig. 5. Contour plots of the calculated two-dimensional (R_1 , R_2) PES at $\gamma = 116.8^\circ$ of the $1A'$ states of ozone: (a) ground state $X'1A'$, (b) $\tilde{C}'1A'$ state and (c) $\tilde{D}'1A'$ state. The difference in contour lines is 1000 cm^{-1} ($\approx 0.124 \text{ eV}$).

In the lower C_s symmetry both states are of A'' symmetry and the previously cited barrier appears for angle values lower than $\gamma = 116.0^\circ$ as a result of the states' interaction leading to a potential well for the $\tilde{A}'1A''$ state (see fig. 8b) for small angles (such as 100°) and a repulsive character of this state for angles about 116° – 125° (see fig. 4b).

For an angle of $\gamma = 100^\circ$ the wavefunction of the $\tilde{A}'1A''$ state between $R_2 = 2.00$ and $2.80 a_0$ (for $R_1 = 2.413 a_0$) is dominated by the configuration $\tilde{J} = \dots 8a'^2 9a'^2 10a'^1 1a''^2 2a''^2 3a''^1$ (one-electron excitation). For $R_2 \geq 2.90 a_0$ the configuration $\tilde{K} = \dots 8a'^2 9a'^1 10a'^2 1a''^2 2a''^2 3a''^1$ is also important and be-

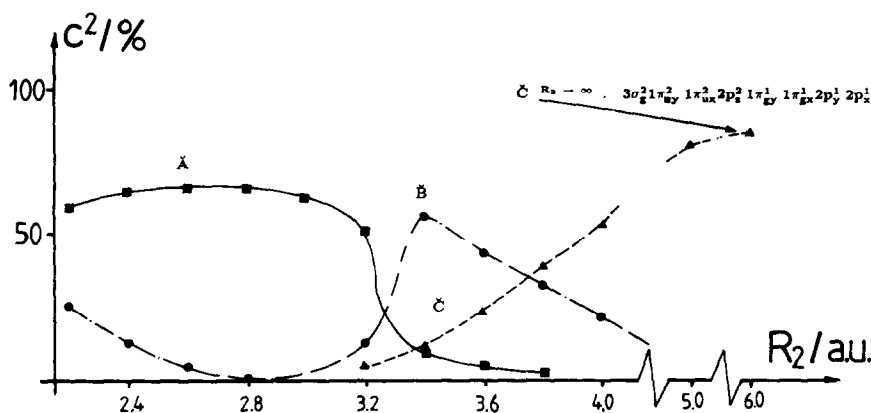


Fig. 6. Description of the ground state X^1A' on the CI level at various internuclear separations R_2 for fixed geometry values ($R_1 = 2.413 a_0$; $\gamma = 116.8^\circ$) as function of the weight C^2 (in percent) in the CI expansion. The configurations are as follows: \hat{A} : $\dots 8a'^2 9a'^2 10a'^2 1a''^2 2a''^2$, \hat{B} : $\dots 8a'^2 9a'^2 10a'^1 11a'^1 1a''^2 2a''^2$, \hat{C} : $\dots 8a'^2 9a'^2 10a'^1 11a'^1 1a''^2 2a''^1 3a''^1$ or at large R_2 : $\dots 1\pi_{ux}^2 1\pi_{uy}^2 1\pi_{gx}^2 1\pi_{gy}^2 1\pi_{ux}^2 1\pi_{gx}^2 2p_z^2 2p_z^2$.

comes the major term for values lower than $R_2 \approx 3.2 a_0$.

At higher angle values (at $R_1 = 2.413 a_0$ and $\gamma = 116.8^\circ$; see table 4) the configuration \hat{J} is dominant between $R_2 = 2.00 a_0$ and $2.413 a_0$; for $R_2 > 2.413 a_0$ the configuration \hat{K} is the most important one until $R_2 \leq 3.20 a_0$. For $R_2 > 3.20 a_0$ (for both angle values $\gamma = 100.0^\circ$ and 116.8°) the four-open-shell configuration $\hat{L} = \dots 8a'^2 9a'^1 10a'^1 11a'^1 1a''^2 2a''^2 3a''^1$ dominates the wavefunction and describes in the dissociation limit at $R_2 = 10.0 a_0$ the $^3P_g(\dots 2p_x^2 2p_y^2 2p_z^1) + X^3\Sigma_g^-(\dots 1\pi_{ux}^2 1\pi_{uy}^2 1\pi_{gx}^1 1\pi_{gy}^1)$ fragmentation.

The vibrational frequencies are calculated as $\nu_1 = 1170 \text{ cm}^{-1}$, $\nu_2 = 573 \text{ cm}^{-1}$ and $\nu_3 = 996 \text{ cm}^{-1}$. The first two values show an excellent agreement with recent experimental values (see table 6).

(ii) The low-lying excited state, \tilde{B}^1A'' , which dissociates to the excited fragments $O(^1D_g) + O_2(a^1\Delta_g)$, has been calculated with a vertical energy of 2.64 eV and with an adiabatic energy of 2.10 eV. As shown in fig. 7c it is a bound state with an equilibrium geometry of $R_1 = R_2 = 2.56 a_0$ and $\gamma = 116.0^\circ$. Its calculated dissociation energy of 1.79 eV has been estimated taking the energy difference between the O_3 minimum and the energy of the fragments $O + O_2(^1\Delta_g)$; see table 6. Between $R_2 = 2.00 a_0$ and $2.413 a_0$ (for $R_1 = 2.413 a_0$ and $\gamma = 116.8^\circ$) the wavefunction is dominated by the configurations \hat{K} and $\hat{M} = \dots 8a'^2 9a'^1 10a'^2 1a''^2 2a''^1 3a''^2$ (two-electron excitation). For $R_2 > 2.413 a_0$ the configuration $\hat{J} =$

$\dots 8a'^2 9a'^1 10a'^2 1a''^2 2a''^2 3a''^1$ is the leading term until $R_2 = 3.20 a_0$. For larger values of R_2 to the dissociation limit ($R_2 = 10.0 a_0$) the wavefunction is dominated by the configuration \hat{L} , but in the present case it describes the $^1D_g(\dots 2p_x^2 2p_y^2 2p_z^1) + a^1\Delta_g(\dots 1\pi_{ux}^2 1\pi_{uy}^2 1\pi_{gx}^1 1\pi_{gy}^1)$ fragmentation.

The vibrational modes have been calculated with the values $\nu_1 = 995 \text{ cm}^{-1}$, $\nu_2 = 426 \text{ cm}^{-1}$ and $\nu_3 = 1024 \text{ cm}^{-1}$. The first two values show an excellent agreement with the experimental values of Levene et al. [17]. The recent experimental values of Anderson et al. [16] are about 18% to 33% higher than our predicted values.

(iii) The high-lying state, \tilde{E}^1A'' has not been investigated on the level of a 3D-PES (see figs. 4a, b). It has a vertical energy of 6.39 eV and it is correlated to the C_{2v} state 2^1A_2 . Similarly as for the low-lying A'' states previously discussed (see also fig. 2) some conical intersections (at least two) are expected due to a crossing between the 2^1A_2 and 2^1B_1 states (see ref. [46]) and complicated 3D-PES as for the \tilde{A}^1A'' and \tilde{B}^1A'' states are predicted. Based on the calculated potential curves the \tilde{E}^1A'' state appears as a repulsive state at $\gamma = 116.8^\circ$; it dissociates into $O(^1D_g) + O_2(a^1\Delta_g)$. In the Franck-Condon region the wavefunction of this state is dominated by the configuration $\hat{N} = \dots 8a'^2 9a'^2 10a'^1 1a''^2 2a''^1 3a''^2$ (two-electron excitation). For $R_2 \geq 3.40 a_0$ the configurations \hat{J} and $\hat{O} = \dots 8a'^1 9a'^2 10a'^1 11a'^1 1a''^2 2a''^1 3a''^2$ (three-electron excitation) are the most impor-

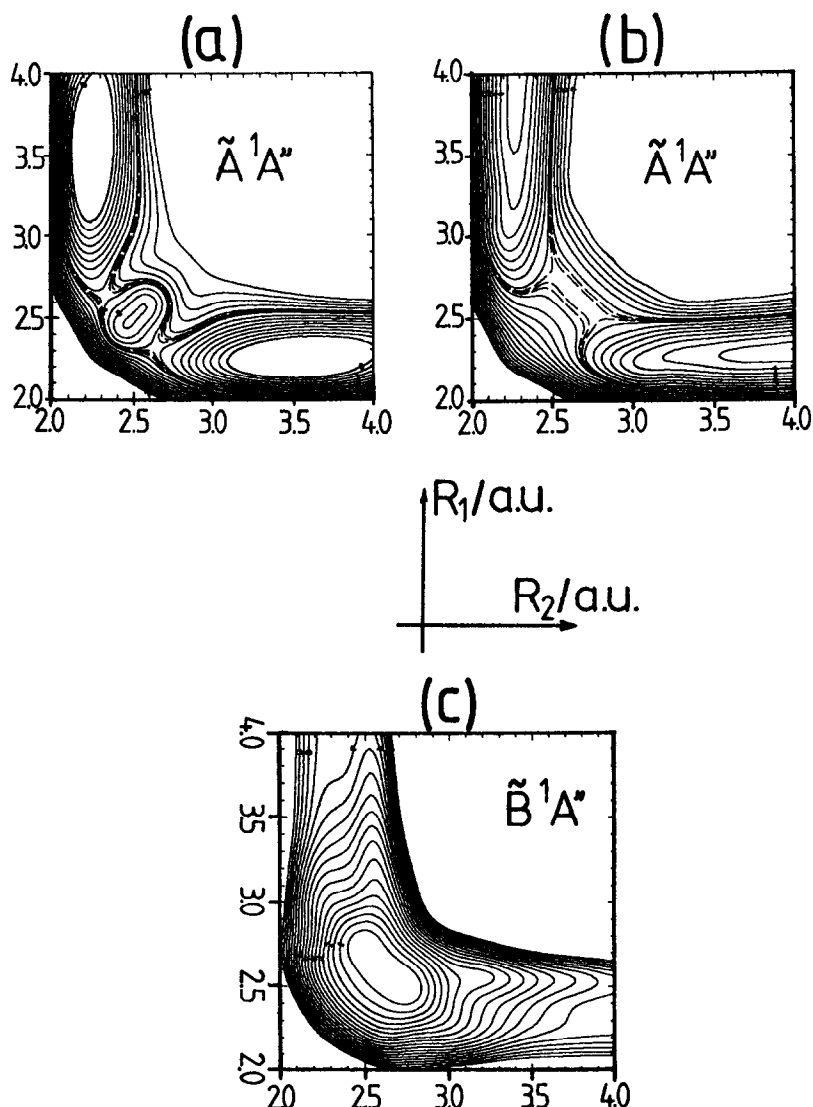


Fig. 7. Contour plots of the calculated two-dimensional (R_1 , R_2) PES of the $^1A''$ states of ozone: (a) \tilde{A}^1A'' at $\gamma=100^\circ$, (b) \tilde{A}^1A'' at $\gamma=116.8^\circ$ and (c) \tilde{B}^1A'' at $\gamma=116.8^\circ$. The difference in contour lines is 1000 cm^{-1} ($\approx 0.124\text{ eV}$).

tant ones. Towards the dissociation limit (at $R=10.0\ a_0$) the fragments are described by the negative linear combination of the configurations $\hat{P}=\dots 8a'^2 9a'^2 10a'^1 11a'^2 1a''^2 2a''^1 3a''^0$ and $\hat{Q}=\dots 8a'^2 9a'^2 10a'^1 11a'^0 1a''^2 2a''^1 3a''^2$ corresponding to $^1D_g(\dots 2p_x^1 2p_y^1 2p_z^2) + a^1\Delta_g(\dots 1\pi_{ux}^2 1\pi_{uy}^2 1\pi_{gx}^0 1\pi_{gy}^2)$ and $^1D_g(\dots 2p_x^1 2p_y^1 2p_z^2) + a^1\Delta_g(\dots 1\pi_{ux}^2 1\pi_{uy}^2 1\pi_{gx}^2 1\pi_{gy}^0)$, respectively.

3.3. Transition moments

As seen in fig. 2 almost all of the low-lying states in the symmetric C_{2v} arrangement are accessible from the X^1A_1 ground state with the exception of the two 1A_2 states. Depending on the symmetry of the upper state, the orientation of the transition moment is different in the various transitions and only one spatial component is always active.

Table 8

Calculated transition moments in terms of the C_{2v} symmetry internal coordinate s_3 for the electronic transitions ${}^1A' \leftarrow X {}^1A'$. Distances s_1 and s_3 are given in a_0 , transition moments μ_i in au and energy differences ΔE relative to the ground state minimum in nm

| | \tilde{C} | | | \tilde{D} | | | \tilde{R} | | |
|----------------------------------|---------------|---------|------------|-------------|--------------|------------|-------------|--------------|------------|
| | μ_y | μ_z | ΔE | μ_y | μ_z | ΔE | μ_y | μ_z | ΔE |
| $s_1 = 3.39, s_2 = 116.8^\circ$ | | | | | | | | | |
| $s_3 = \pm 0.007$ | ± 0.0054 | 0.0009 | 283 | 0.9770 | ± 0.0920 | 228 | 0.5090 | ± 0.0402 | 183 |
| $s_3 = \pm 0.2828$ | ± 0.0310 | 0.0024 | 250 | 0.8560 | ± 0.1590 | 230 | 0.2690 | ± 0.0382 | 191 |
| $s_3 = \pm 0.5656$ | ± 0.2550 | 0.0730 | 207 | 0.5200 | ± 0.1100 | 201 | 0.1600 | ± 0.0338 | 151 |
| $s_1 = 3.677, s_2 = 116.8^\circ$ | | | | | | | | | |
| $s_3 = \pm 0.007$ | ± 0.00014 | 0.0017 | 342 | 0.710 | ± 0.1100 | 296 | 0.3240 | ± 0.0286 | 224 |
| $s_3 = \pm 0.2828$ | ± 0.0101 | 0.0022 | 329 | 0.643 | ± 0.0880 | 314 | 0.2090 | ± 0.0238 | 231 |
| $s_3 = \pm 0.5656$ | ± 0.1450 | 0.0311 | 304 | 0.390 | ± 0.0140 | 295 | 0.0954 | ± 0.0393 | 260 |

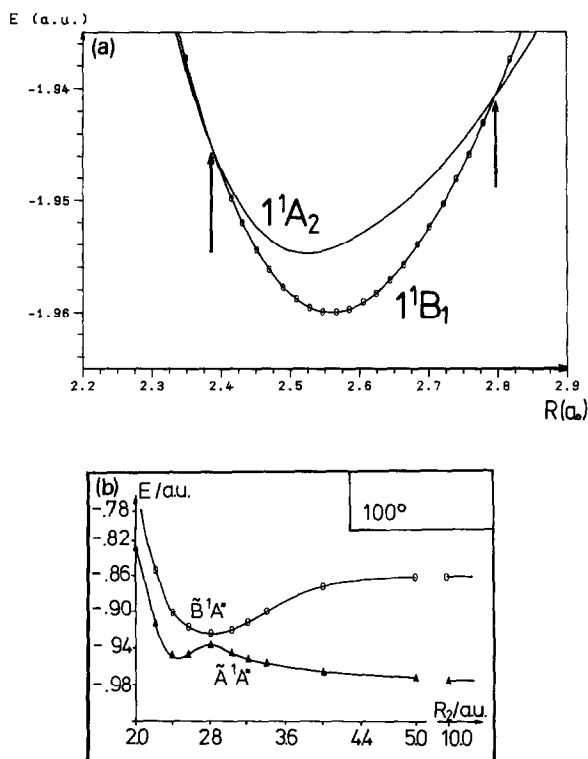


Fig. 8. Potential energy curves for the two lowest-lying excited singlet states in ozone: (a) in C_{2v} symmetry (see also ref. [46]) there are two crossings between the 1^1B_1 and 1^1A_2 states as function of the bond length $R_1 = R_2 = R$ whereby bond angle γ is held at 116° ; (b) in C_s symmetry there is an avoided crossing of potential curves of $\tilde{A} {}^1A'$ and $\tilde{B} {}^1A''$ states as function of R_2 , whereby $R_1 = 2.413 a_0$ and $\gamma = 100^\circ$.

A slight asymmetric distortion of the nuclear framework makes transitions to all states allowed according to the C_s dipole selection rules. The ${}^1A''$ states which correlate with the 1A_2 states, become accessible by vibronically induced transitions. For the ${}^1A'$ states the transition moment possesses now two spatial components; one is the “electronically allowed” component based on C_{2v} selection rules and the other the “vibronically allowed” component.

For the actual evaluation of the various transition moments the C_{2v} symmetry internal coordinates defined as

$$s_1(A_1) = (R_1 + R_2)/\sqrt{2},$$

$$s_2(A_1) = \gamma,$$

$$s_3(B_2) = (R_1 - R_2)/\sqrt{2} \quad (6)$$

are employed. Transition moments are computed for three asymmetric distortions ($|\Delta R| = 0.01, 0.4, 0.8 a_0$) corresponding to values for the s_3 coordinate of $\pm 0.007, \pm 0.2828$ and $\pm 0.567 a_0$; s_1 was generally 3.39 and $3.677 a_0$ and γ was chosen as 116.8° or 100° for most investigations. The computed data are listed in table 8 for the ${}^1A'$ states and in table 9 for those of A'' symmetry. The transition moments are even functions with respect to s_3 for all “electronically allowed” species, while the “vibronically allowed” components are asymmetric with respect to $s_3 = 0$, as indicated in the tables.

By far the strongest transition moments are found for the transition $\tilde{D} {}^1A' \leftarrow X {}^1A'$, followed by the transition $\tilde{R} {}^1A' \leftarrow X {}^1A'$. The dominant spatial compo-

Table 9

Calculated transition moments for the electronic transitions ${}^1\text{A}'' \leftarrow \tilde{\text{X}} {}^1\text{A}'$. Distances s_1 and s_3 are given in a_0 and transition moments in au

| | $\tilde{\text{A}}$ μ_x | $\tilde{\text{B}}$ μ_x | $\tilde{\text{E}}$ μ_x |
|----------------------------------|-------------------------------|-------------------------------|-------------------------------|
| $s_1 = 3.39, s_2 = 100^\circ$ | | | |
| $s_3 = \pm 0.007$ | ± 0.0007 | 0.0190 | – |
| $s_3 = \pm 0.2828$ | ± 0.0034 | 0.0215 | – |
| $s_3 = \pm 0.5657$ | ± 0.0042 | 0.0022 | – |
| $s_1 = 3.677, s_2 = 100^\circ$ | | | |
| $s_3 = \pm 0.007$ | ± 0.0026 | 0.0072 | – |
| $s_3 = \pm 0.2828$ | ± 0.0066 | 0.0150 | – |
| $s_3 = \pm 0.5657$ | ± 0.0055 | 0.0010 | – |
| $s_1 = 3.39, s_2 = 116.8^\circ$ | | | |
| $s_3 = \pm 0.007$ | ± 0.0125 | 0.0110 | ± 0.0351 |
| $s_3 = \pm 0.2828$ | ± 0.0153 | 0.0068 | ± 0.0474 |
| $s_3 = \pm 0.5657$ | ± 0.0003 | 0.0008 | ± 0.0355 |
| $s_1 = 3.677, s_2 = 116.8^\circ$ | | | |
| $s_3 = \pm 0.007$ | ± 0.0062 | 0.00341 | ± 0.0316 |
| $s_3 = \pm 0.2828$ | ± 0.0076 | 0.00136 | ± 0.0440 |
| $s_3 = \pm 0.5657$ | ± 0.0011 | 0.0002 | ± 0.0490 |

nent is the “electronically allowed” μ_y dipole transition (corresponding to the $\text{X } {}^1\text{A}_1 \rightarrow {}^1\text{B}_2$ transition in C_{2v} symmetry, fig. 2) while the vibronically induced μ_z component is quite weak in the geometry range studied and causes in the main a shift in the orientation of the total transition dipole between 5° and 12° relative to μ_y ($\delta = |\arctan(\mu_z/\mu_y)|$). The large transition moment for the $\tilde{\text{D}} \rightarrow \tilde{\text{X}}$ transition is expected on the basis of qualitative arguments since this is a $\pi \rightarrow \pi^*$ type transition for which both orbitals have their maximum charge density in the same plane. At nearly vertical excitation ($s_1 = 3.39 a_0$, $s_2 = 116^\circ$ and $s_3 = \pm 0.007 a_0$) the calculated oscillator strength is $f_e = 0.13$ in comparison with the experimentally deduced value of 0.1 [21]. For the $\tilde{\text{R}}$ state the calculations find $f_e = 0.04$. Outside of the Franck–Condon region μ_y decreases for both states as is obvious from table 8. This pattern is caused in the main by interaction with other states (fig. 4). Since the $\tilde{\text{R}}$ state is the highest state treated, its mixing with other states has not been investigated in detail; the dominant perturber for the $\tilde{\text{D}}$ state is the $\tilde{\text{C}}$ state.

For the $\tilde{\text{C}}$ state, which correlates in the Franck–Condon area with $2 {}^1\text{A}_1$, the “electronically allowed”

component μ_z is quite weak (see also ref. [46]) since it results from a double excitation ($6a_1 4b_2 \rightarrow 2b_1^2$ in C_{2v} , $9a' 10a' \rightarrow 3a''^2$ in C_s) relative to the ground state. The calculated oscillator strength for nearly vertical transition is only $f_e = 0.03 \times 10^{-4}$ (exp. $\approx 1.0 \times 10^{-4}$ [21]). Outside of the Franck–Condon area both components of the transition moment are active, whereby for large values of s_3 the μ_y component becomes quite sizeable due to the interaction with the $\tilde{\text{D}}$ state (fig. 4, table 8). In the energy range $\lambda = 202\text{--}207 \text{ nm}$ (5.98–6.15 eV), the $\tilde{\text{C}}$ and $\tilde{\text{D}}$ state geometry is close to $s_1 = 3.394 a_0$ and $s_3 = 0.565 a_0$ (corresponding to $R_1 = 2.0 a_0$, $R_2 = 2.8 a_0$, $\gamma = 116.8^\circ$); the calculated values are $f_e = 0.01$ ($\tilde{\text{C}}$) and $f_e = 0.04$ ($\tilde{\text{D}}$) and represent about 8% and 31% of the total value ($f_e = 0.13$) computed for the Hartley band. It should be noted, however, that in this energy range both states possess repulsive character and lie above the $\text{O}({}^1\text{D}_g) + \text{O}_2(\text{a } {}^1\Delta_g)$ dissociation limit.

The perpendicular transition moments to the three A'' states are small. The $\tilde{\text{E}}$ state corresponds in the main to $2 {}^1\text{A}_2$ in the symmetric nuclear arrangement, so that μ_x must be considered as a vibronically induced moment with an asymmetric behavior in the s_3 coordinate. This state has not been analyzed in detail and will thus not be discussed further. In the Franck–Condon area are the computed value is $f_e = 0.2 \times 10^{-3}$.

The understanding of the behavior of μ_x for the $\tilde{\text{A}}$ and $\tilde{\text{B}}$ state is much more complicated since both states show heavy mixing in the lower C_s symmetry (figs. 2 and 4), the amount of which varies with geometrical parameters. For $\gamma = 100^\circ$ the identification of $\tilde{\text{A}}$ with its C_{2v} analogue ${}^1\text{A}_2$ ($4b_2 \rightarrow 2b_1$) seems clear according to the angular potential curves shown in figs. 3 and 6 of ref. [46], at least up to R_2 values of $2.8 a_0$. For this reason μ_x ($\tilde{\text{A}}$) is the vibronically induced moment and μ_x ($\tilde{\text{B}}$) is the “electronically allowed” transition corresponding to the $\text{X } {}^1\text{A}_1 \rightarrow {}^1\text{B}_1$ ($6a_1 \rightarrow 2b_1$) transition in the symmetric arrangement, showing the symmetric behavior with the coordinate s_3 . This area ($\gamma = 100^\circ$) is also of special importance for the $\tilde{\text{A}}$ state since this state possesses its absolute minimum around $\gamma = 100^\circ$ (fig. 7, table 5).

For $\gamma = 116.8^\circ$ the situation is much more complex and a definitive correlation to one or the other of the C_{2v} symmetry states is difficult because (a) both states are very close in energy (fig. 8a) and change

their relative ordering with geometry, (b) the actual degree of mixing in the lower symmetry depends to some extent on the technical treatment, and (c) the $6a_1$ and $4b_2$ MO which characterize the C_{2v} states change their stability order between 130° and 100° and the optimal MO in the C_s SCF procedure is a combination of both. We will therefore base the qualitative reasoning on the $\gamma=100^\circ$ data. In previous work [44] the calculated transition moments to the lowest $^1A'$ states have been found to be of similar magnitude for $R_1=R_2$ and fixed angle γ . In the present work exact C_{2v} geometries are not considered in calculating transition moments but only slight geometrical deviations therefrom; the results show that the magnitude of the transition moments to these states is also similar in the Franck–Condon region.

The $\tilde{B}-\tilde{X}$ transition probability is much smaller than that of the $\tilde{D}-\tilde{X}$ transition because the states are connected by an excitation from an in-plane ($6a_1$) to an out-of-plane ($2b_1$) orbital. The maximum seems to be not in the symmetric arrangement (at least not for $\gamma=100^\circ$) but rather for the asymmetrical distorted geometry ($s_3=0.2828$). The calculated oscillator strength for the vertical transition is $f_e=2.3\times 10^{-5}$ (exp. 3.2×10^{-5} [53]); its dependence on bending is discussed elsewhere [15,44,46]. The intensity of the vibronically induced transition $\tilde{A}-\tilde{X}$ increases with asymmetric distortion.

4. Simulation of spectral bands

Based on the preceding potential energy data and the calculated transition moment a simple simulation of the band spectra is attempted. Various alternative assignments to the known spectral lines are made, and the calculated results should stimulate further experimental studies in the search for hidden or weak lines; the long-range goal of the experimental and theoretical efforts is, of course, the unequivocal assignment of all the peaks in the entire ozone spectrum.

The simulation of the absorption bands is based on the golden rule for electric dipole transitions, according to which the transition moment between lower state (marked by a double prime) and higher state (marked by a single prime) is given as

$$R_{n'n''e'e''} = |\langle \chi_{n'}(s_i)^{IR} | \langle \psi_{e'} | (\epsilon \cdot \phi)^{IR} \times \psi_{e''} \rangle | \chi_{n''}(s_i)^{IR} \rangle|^2. \quad (7)$$

Here the χ functions are the vibrational functions given in terms of the C_{2v} symmetry internal coordinates (eq. (6)), which describe (in an uncoupled approximation) the nuclear motion, i.e. the vibrational modes. ψ are the electronic wavefunctions, ϵ is the vector of polarization of the photon and ϕ the electric dipole moment operator. The superscript IR denotes the corresponding irreducible representation of the wavefunctions and the transition dipole component, if convenient. The intensity of the calculated lines which is proportional to the absorption cross section, is given by

$$I_{(\nu_1\nu_2\nu_3)' \leftarrow (000)''} = A(\nu'_1, \nu''_1) B(\nu'_2, \nu''_2) C(\nu'_3, \nu''_3), \quad (8)$$

with

$$A(\nu'_1, \nu''_1) = |\langle \chi_{\nu'_1}(s_1) | \chi_{\nu''_1}(s_1) \rangle|^2, \quad (9a)$$

$$B(\nu'_2, \nu''_2) = |\langle \chi_{\nu'_2}(s_2) | \chi_{\nu''_2}(s_2) \rangle|^2, \quad (9b)$$

$$C(\nu'_3, \nu''_3) = |\langle \chi_{\nu'_3}(s_3) | \langle \psi_{e'} | (\epsilon \cdot \mu) | X^1A' \rangle | \chi_{\nu''_3}(s_3) \rangle|^2. \quad (9c)$$

The terms $A(\nu'_1, \nu''_1)$ and $B(\nu'_2, \nu''_2)$ are the Franck–Condon factors between the vibrational wavefunctions in their corresponding internal coordinates for the symmetric stretching mode ν_1 and bending mode ν_2 , respectively. Depending on the symmetry of the electronic excited state the term $C(\nu'_3, \nu''_3)$ describes a vibronically allowed transition, an electronically allowed transition or both. A shortcoming of this approach is certainly the neglect of coupling between the various modes.

Considering the ground state in its zero-point levels, the intensity is given (in $(\text{au})^2$) by

$$I_{(\nu_1\nu_2\nu_3)' \leftarrow (000)''} = A(\nu'_1, 0) B(\nu'_2, 0) \times |\langle \chi_{\nu'_3}(s_3)^{(A_1, B_2)} | \langle \psi_{e'} | (\epsilon \cdot \phi)^{IR} | X^1A' \rangle \times | \chi_{\nu''_3}(0)^{A_1} \rangle|^2. \quad (10)$$

The vibrational functions are those used for the calculation of the vibrational modes (see table 6).

4.1. The Wulf absorption band

As discussed in the preceding sections the \tilde{A}^1A'' is a metastable bound state separated from the dissociation continuum by a barrier. The transition $\tilde{A}^1A'' \leftarrow X^1A'$ becomes vibronically allowed with the transition moment μ_x as shown in table 9. The matrix element $C(\nu_3', 0)$ of eq. (9c) does not vanish for the transitions $\nu_3' = 1, 3 \dots \leftarrow \nu_3'' = 0$. In analogy to the interpretation of the Huggins absorption band by Brand et al. [21] and Katayama [20], hot bands are also considered in the present study. From experi-

mental investigations of ozone in its ground state [21,48], s_1 and s_3 modes are strongly coupled, making $\Delta\nu_3$ transitions more likely. Hence it is assumed, that if $\Delta\nu_3$ transitions are possible in the cold spectrum, $\Delta\nu_3$ transitions are also possible in the hot bands, for example $\nu_3' = 0, 2 \dots \leftarrow \nu_3'' = 1, 3$. Taking this into account, our ab initio simulation would interpret the lowest transitions in the Wulf bands as hot bands. In the actual simulation the calculated energies for the \tilde{A}^1A'' state are shifted by 0.2 eV to lower energies, so that the origin is positioned at $E_{001} = 11128 \text{ cm}^{-1}$, placing the zero-point level of the

Table 10

Calculated band line positions for the $\tilde{A}^1A'' \leftarrow X^1A'$ transition in comparison with the experiment. Band position in cm^{-1} and intensity in $(\text{au})^2$

| Experiment | | | | | Present work | | | |
|-------------------|-------|-------|-----------------------|--|--------------------------|------------------------|--|--|
| [7] ^{a)} | [13] | [12] | [15,16] ^{b)} | assigned progression $(\nu_1\nu_21)' \leftarrow (000)''$ | calculated line position | intensity | assigned progression $(\nu_1\nu_21)' \leftarrow (000)''$ | expected hot lines progression ^{c)} |
| – | – | – | – | – | 9028 | 0.29×10^{-12} | – | 000 ← 001 |
| – | – | 9544 | – | 001 | 9601 | 0.23×10^{-11} | – | 010 ← 001 |
| | | | | | 9647 | 0.93×10^{-12} | – | 001 ← 020 |
| 10000 | 10091 | 10078 | – | 011 | 10000 | 0.70×10^{-12} | – | 001 ← 100 |
| | | | | | 10096 | 0.73×10^{-12} | – | 100 ← 001 |
| | | | | | 10159 | 0.89×10^{-12} | – | 020 ← 001 |
| – | – | – | – | – | 10387 | 0.11×10^{-10} | – | 001 ← 010 |
| 10567 | 10571 | 10588 | – | 021 | 10575 | 0.56×10^{-12} | – | 011 ← 100 |
| | | | | | 10669 | 0.18×10^{-12} | – | 110 ← 001 |
| – | – | – | – | – | 10961 | 0.63×10^{-10} | – | 011 ← 010 |
| 11133 | 11093 | 11128 | – | 031 | 11128 | 0.62×10^{-10} | 001 | – |
| | | | | | 11133 | 0.44×10^{-10} | – | 021 ← 100 |
| | | | | | 11227 | 0.22×10^{-11} | – | 120 ← 001 |
| | | | | | 11233 | 0.37×10^{-10} | – | 040 ← 001 |
| 11700 | 11669 | 11701 | – | 041 | 11700 | 0.50×10^{-9} | 011 | – |
| | | | | | 11750 | 0.47×10^{-10} | – | 050 ← 001 |
| 12267 | 12240 | 12246 | – | 051 | 12195 | 0.16×10^{-9} | 101 | – |
| | | | | | 12295 | 0.19×10^{-8} | 021 | – |
| 12834 | – | – | 12750 | – | 12770 | 0.12×10^{-8} | 111 | – |
| | | | | | 12802 | 0.46×10^{-8} | 031 | – |
| 13400 | – | – | 13325 | – | 13327 | 0.48×10^{-8} | 121 | – |
| | | | | | 13332 | 0.79×10^{-8} | 041 | – |
| 13967 | – | – | 13875 | – | 13837 | 0.16×10^{-8} | 211 | – |
| | | | | | 13850 | 0.10×10^{-7} | 051 | – |
| | | | | | 13870 | 0.12×10^{-7} | 131 | – |
| 14534 | – | – | 14450 | – | 14358 | 0.97×10^{-8} | 061 | – |
| | | | | | 14395 | 0.60×10^{-8} | 221 | – |
| | | | | | 14440 | 0.20×10^{-7} | 141 | – |

^{a)} Original values of Wulf [7] given from the formula $E_{001} = 10000 + 566.7 \nu_2$ in cm^{-1} for $\nu = 0-9$.

^{b)} The values from refs. [15,16] have been graphically estimated.

^{c)} Calculated for room temperature $T = 300 \text{ K}$.

Table 11

Calculated band line positions for the transition $\tilde{B}^1A'' \leftarrow X^1A'$ in comparison with experiment. Band position in cm^{-1} and intensity in $(\text{au})^2$. Listed is the progression $(\nu_1\nu_2\nu_3)' \leftarrow (000)''$

| Experiment | | | | | Present work | | |
|-------------------|-------|-------|--------------------|-------|-----------------------------|-----------------------|---|
| [7] ^{a)} | [19] | [17] | [53] ^{b)} | [16] | calculated line position | intensity | assigned progression $(\nu_1\nu_2\nu_3)'$ |
| — | — | — | 15310 | — | — | — | — |
| 16190 | — | — | 15850 | — | — | — | — |
| 16625 | 16613 | — | 16656 | 16600 | 16707 | 0.12×10^{-4} | 000 |
| 17270 | 17381 | 17409 | 17454 | 17414 | 17133 | 0.20×10^{-5} | 010 |
| 17704 | — | — | — | 17714 | 17702 | 0.21×10^{-4} | 100 |
| 18308 | — | — | — | 18320 | 18128 | 0.33×10^{-5} | 110 |
| 18743 | 18729 | 18806 | — | 18790 | 18690 | 0.24×10^{-4} | 200 |
| 19307 | — | — | — | 19361 | 19116 | 0.33×10^{-5} | 210 |
| 19742 | 19765 | 19699 | — | 19792 | 19671 | 0.28×10^{-4} | 300 |
| 20266 | — | — | — | 20344 | 20204 | 0.24×10^{-5} | 310 |
| 20701 | 20706 | 20681 | — | 20733 | 20646 | 0.95×10^{-5} | 400 |
| 21186 | 21234 | — | — | 21260 | 21072 | 0.13×10^{-5} | 410 |
| 21620 | 21648 | 21550 | — | — | 21612 | 0.35×10^{-5} | 500 |
| 22065 | — | — | — | — | 22038 | 0.60×10^{-6} | 510 |
| 22500 | — | 22545 | — | — | 22567 | 0.17×10^{-5} | 600 |
| 22905 | — | — | — | — | 22993 | 0.23×10^{-6} | 610 |
| 23340 | — | — | — | — | 23498 | 0.60×10^{-6} | 700 |

^{a)} Original values of Wulf [7] from the formula $E_{000} = 16625 + n' (1099 - 20n') - 435 n''$; $n' = 1-7$, $n'' = 0, 1$.

^{b)} Values from cold-phase experiments.

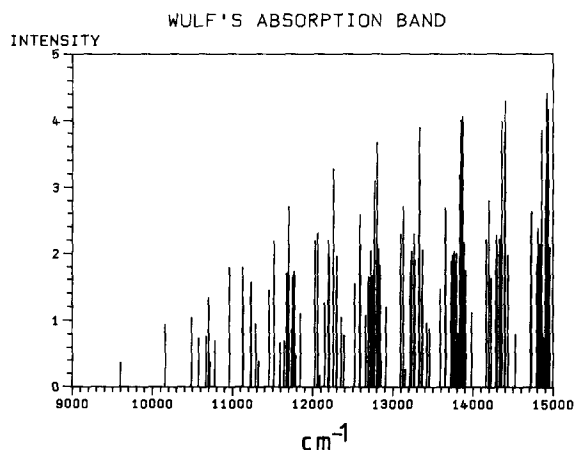


Fig. 9. Simulated Wulf absorption band using calculated band line intensities (shown in arbitrary units; see table 10 for absolute values) on the basis of the transition $\tilde{A}^1A'' \leftarrow X^1A'$ as function of the photoexcitation energy (in cm^{-1}).

excited state at $E_{000} = 10070 \text{ cm}^{-1}$. The calculated values for the intensity and our alternative assignments are listed in table 10; the resulting spectrum of the simulated band is shown in fig. 9.

The calculations show that the first experimental peaks can also be interpreted as hot bands coming from ground state vibrational excited states $\nu_1'' = 1$, $\nu_2'' = 2$ and $\nu_3'' = 1$. Moreover, the intensity of the peaks increases with increasing excitation energy as expected from experiment. The progressions have been considered up to the top of the barrier ($E \approx 14500 \text{ cm}^{-1}$).

4.2. The Chappuis absorption band

The electronically allowed transition $\tilde{B}^1A'' \leftarrow X^1A'$ describes excitations into a potential well of a bound state which possesses an equilibrium angle similar to the ground state. The calculated intensities and band line positions of this transition are listed in table 11 and the simulated spectra up to excitation energies of 28000 cm^{-1} are shown in fig. 10a. The calculated ab

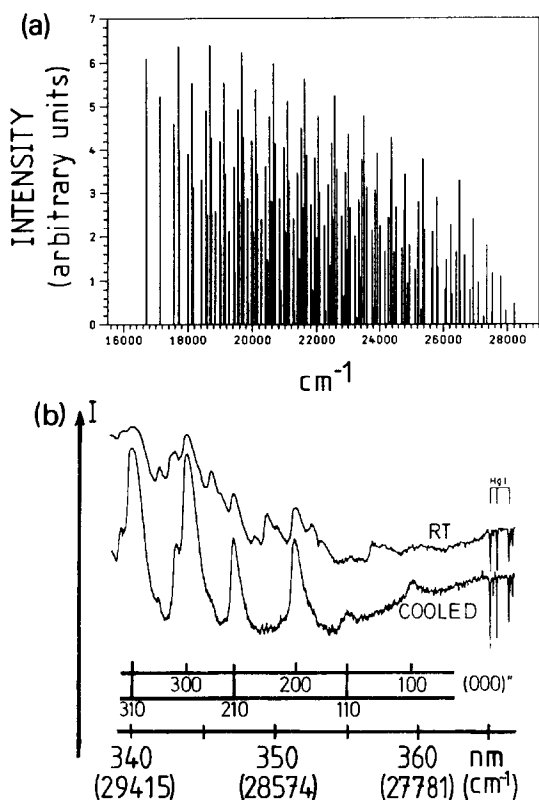


Fig. 10. (a) Simulated Chappuis absorption band using calculated band line intensities (see table 11 for absolute values) described by the transition $\tilde{B}^1A'' \leftarrow X^1A'$ as function of the photoexcitation energy (in cm^{-1}); (b) observed absorption cross section for the falloff regions of the Chappuis and Huggins absorption bands obtained by Katayama [20]; see text for details.

initio value for the origin of the \tilde{B}^1A'' state has been shifted in this simulation to higher energy values by 50 cm^{-1} arriving at 16700 cm^{-1} .

The results show that the principal progression can be described by $(v_1, v_2, 0)' \leftarrow (000)''$ with $v_1=0-11$ for $v_2=0, 1$. Moreover the intensity of the progressions decreases for increasing photoexcitation energies. The maximum of the progressions is found to be for $(v_1, 0, 0)' \leftarrow (000)''$ with $v_1=1, 2$.

The simulation of the hot bands for this band predicts relatively small values compared to the intensities of the cold band.

In an experimental study of the Huggins absorption band Katayama [20] has reported two new bands in the "cooled spectrum". They are shown in fig. 10b. He has assigned these bands as the transi-

tions $(110)' \leftarrow (000)''$ (at $\lambda \approx 360 \text{ nm}$) and $(100)' \leftarrow (000)''$ (at $\lambda \approx 355 \text{ nm}$) of the Huggins band. Considering the reported spectra as function of energy (see fig. 10b) the observed peaks for "cooled ozone" decrease in intensity for increasing photoexcitation energy, contrary to the generally known behavior of the Huggins band ($\lambda < 355 \text{ nm}$) [9,10]. Based on the results of the present work these two observed peaks can alternatively be interpreted as the progression $(v_1, v_2, 0)' \leftarrow (000)''$ for large values $v_1 \geq 10$ and $v_2 \geq 3$ describing the blue "falloff" limit of the Chappuis band, i.e. it can be expected that in this energy region an overlap between the Chappuis band and the Huggins band exists.

4.3. The transition $\tilde{C}^1A' \leftarrow X^1A'$

This transition possesses two components of which the vibronically induced (μ_v) is larger in various regions of the PES than the electronically allowed. The calculation for the simulated band line positions shows that the term $C(v_3=1, v_3'=0)$ in eq. (9c) is about two times stronger than $C(v_3=0, v_3'=0)$. The calculated intensities and band line positions are contained in table 12 and shown in fig. 11. The calculated ab initio value for the origin of the \tilde{C}^1A' state has been shifted about 500 cm^{-1} to higher energies to agree with the experimental value 28465 cm^{-1} . The progression has been considered up to the top of the barrier ($E \approx 30600 \text{ cm}^{-1}$) of this state, the latter results from coupling with the strong absorbing state \tilde{D}^1A' . The strong lines have been assigned to the vibrational transitions $(v_1v_2)' \leftarrow (000)''$ of the \tilde{D}^1A' state for $v_1=0-2$ and $v_2=0, 1$. No coupling between the excited states \tilde{C} and \tilde{D} has been considered, however. The zero-point energy of the \tilde{D} state has been shifted by 1550 cm^{-1} to lower energies to match the experimental value 29082 cm^{-1} .

The results show that the weakest progressions can be assigned as $(v_1v_2v_3)' \leftarrow (000)''$ with $v_1=0-2$, $v_2=0-3$ and $v_3=0, 1$. Because the theoretical value for the v_1 vibrational mode is larger than v_3 in the excited state the assignment for the experimental lines $(001)'$, $(110)''$ and $(011)'$ are inverted as the $(100)'$, $(011)'$ and $(110)'$ vibrational transitions, respectively. In agreement with experiment, the calculated intensities become stronger for increasing photoexcitation energy. The calculated line positions

Table 12

Calculated band line positions in comparison with the experiment for the transitions $\tilde{C}^1A' \leftarrow X^1A'$ and $\tilde{D}^1A' \leftarrow X^1A'$ in the energy range of the Huggins absorption band. Band line position in cm^{-1} and intensity in $(\text{au})^2$. Listed are the progressions for $(\nu_1\nu_2\nu_3)' \leftarrow (000)''$

| Experiment | | | | Present work | | | | | |
|------------|-------|-------|---|----------------------------------|----------------------|---|----------------------------------|-----------|---|
| [23] | [21] | [20] | assigned ^{a)} progression from ref. [15] | $\tilde{C}^1A' \leftarrow X^1A'$ | | | $\tilde{D}^1A' \leftarrow X^1A'$ | | |
| | | | | calculated line position | intensity | assigned progression ($\nu_1\nu_2\nu_3$)' | calculated line position | intensity | assigned progression ($\nu_1\nu_2\nu_3$)' |
| 28469 | 28447 | 28465 | 000 | 28465 | 0.3×10^{-8} | 000 | — | — | — |
| 28797 | 28784 | 28803 | 010 | 28797 | 0.6×10^{-8} | 010 | — | — | — |
| 29081 | 29054 | 29082 | 100 | — | — | — | 29082 | 0.01 | 000 |
| 29141 | 29127 | 29146 | 001 | 29125 | 0.6×10^{-8} | 001 | — | — | — |
| | | | | 29136 | 0.2×10^{-8} | 020 | — | — | — |
| | | | | 29153 | 0.1×10^{-7} | 100 | — | — | — |
| 29406 | 29390 | 29412 | 110 | 29420 | 0.5×10^{-9} | 030 | — | — | — |
| | | | | 29457 | 0.1×10^{-7} | 011 | — | — | — |
| 29467 | 29467 | — | 011 | 29485 | 0.2×10^{-7} | 110 | — | — | — |
| 29668 | 29639 | 29660 | 200 | 29769 | 0.2×10^{-8} | 200 | 29607 | 0.02 | 001 |
| 29748 | 29711 | 29724 | 101 | 29796 | 0.3×10^{-8} | 021 | — | — | — |
| | | | | 29814 | 0.2×10^{-7} | 101 | — | — | — |
| — | 29807 | — | 002 | 29824 | 0.6×10^{-8} | 120 | — | — | — |
| 29971 | 29953 | 29974 | 210 | 30080 | 0.1×10^{-8} | 031 | 29851 | 0.03 | 100 |
| | | | | 30101 | 0.4×10^{-7} | 210 | — | — | — |
| 30007 | 30030 | 30036 | 111 | 30108 | 0.2×10^{-8} | 130 | — | — | — |
| | | | | 30146 | 0.2×10^{-8} | 111 | — | — | — |
| 30215 | 30184 | 30209 | 300 | — | — | — | 30377 | 0.04 | 101 |
| 30288 | 30264 | 30277 | 201 | 30429 | 0.4×10^{-7} | 201 | — | — | — |
| — | 30334 | — | 102 | 30440 | 0.1×10^{-7} | 220 | — | — | — |
| | | | | 30485 | 0.1×10^{-7} | 121 | — | — | — |
| 30510 | 30479 | 30509 | 310 | — | — | — | 30621 | 0.05 | 200 |

^{a)} This assignment differs from ref. [20] for ν_1^* by $\nu_1 = \nu_1^* - 2$.

for the transition to \tilde{C} deviate less than 100 cm^{-1} from the measured numbers.

The vibrational transitions to the \tilde{D} state show that they are about 10^6 times stronger than to the \tilde{C} state but no quantitative significance should be attached to this ratio because both states have been considered independently, i.e. the nonadiabatic coupling between both states has been neglected. Moreover, the matrix element $B(\nu_2'=0, \nu_2''=0)$ in eq. (9) for the bending vibrational mode of the \tilde{D} state has been calculated too high ($\nu_2=612 \text{ cm}^{-1}$), differing about two times from the experimental value. The simulation of the hot bands for the transitions to the excited states \tilde{C} and \tilde{D} add in both cases to the intensity of the values $(\nu_1\nu_2\nu_3)$ considered.

5. The potential energy surfaces of the triplet states

For the calculation of the 2D-PES of the triplet states the set of gridpoints is the same as employed for the singlet states. Only the angle values $\gamma=100^\circ$ and 116° have been considered, however, and only the four lowest electronic states are treated at the standard level of accuracy.

The calculated potential curves for the variable R_2 and $R_1=2.413 a_0$ are shown in fig. 12 for $\gamma=100^\circ$ and in fig. 13 for $\gamma=116.8^\circ$. The character of the wavefunctions for these states is summarized in table 13. The characterization of the states as obtained from the 2D-PES is given in table 14. The 2D-PES corresponding to the stretching of the O–O bond lengths (R_1, R_2) for the \tilde{a}^3A' and \tilde{b}^3A'' states at $\gamma=100^\circ$ are

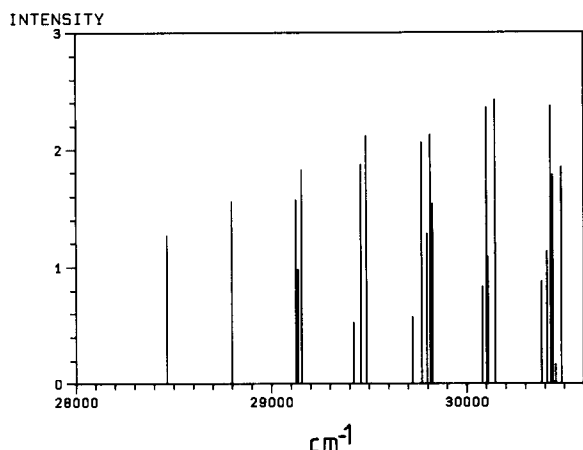


Fig. 11. Simulated Huggins weak absorption band using calculated band line intensities (see table 12 for absolute values) described by the transition $\tilde{C}^1A' \leftarrow X^1A'$ as function of the photoexcitation energy (in cm^{-1}).

shown in figs. 14a and 14b, respectively, and for the \tilde{a}^3A' , \tilde{b}^3A'' , \tilde{c}^3A'' and \tilde{d}^3A' states at $\gamma=116.8^\circ$ in figs. 15a–15d, respectively. They show the following characteristics:

(i) The lowest-lying state for vertical excitations is the \tilde{a}^3A' with 1.67 eV. The corresponding C_{2v} state is the 1^3B_2 (see fig. 3 and table 3). In the dissociation limit it correlates with the $O(^3P_g) + O_2(X^3\Sigma_g^-)$

fragmentation. The PES show that for both angle values considered this state is repulsive, i.e. not bound. Considering the results of a previous work [42] it is expected that this state is weakly bound in the range of $\gamma=105^\circ$ – 110° .

Between $R_2=2.0 a_0$ and $R_2 \leq 3.4 a_0$ (for $R_1=2.413 a_0$ at both angle values) the wavefunction of this state is dominated by the two-open-shell configuration $\hat{F}=\dots 8a'^2 9a'^2 10a'^2 1a''^2 2a''^1 3a''^1$ (one-electron excitation). For $R_2 > 3.4 a_0$ the configuration \hat{C} dominates in the entire range of the PES considered. Near the dissociation limit ($R_2=10.0 a_0$) it describes the fragments in the same manner as has been discussed for the ground state.

(ii) The electronic state \tilde{b}^3A'' is the lowest-lying excited state in ozone. Its absolute minimum calculated at $R_1=R_2=2.57 a_0$ and $\gamma=100.0^\circ$ (fig. 14b) is energetically about 0.90 eV above the global minimum of the ground state. This state correlates with the dissociation channel $O(^3P_g) + O_2(X^3\Sigma_g^-)$ (see fig. 3) leading to a computed dissociation energy as difference between the O_3 minimum and the energy of the diatomic $O_2(X^3\Sigma_g^-)$ at optimal bond length plus an oxygen atom of $D'_e \approx 0.19$ eV.

In contrast to the singlet \tilde{A}^1A'' state for $\gamma=100.0^\circ$ no potential barrier resulting from the configuration interaction between the \tilde{b}^3A'' and \tilde{c}^3A'' is found; from the treatment of the corresponding states $1^3A''$

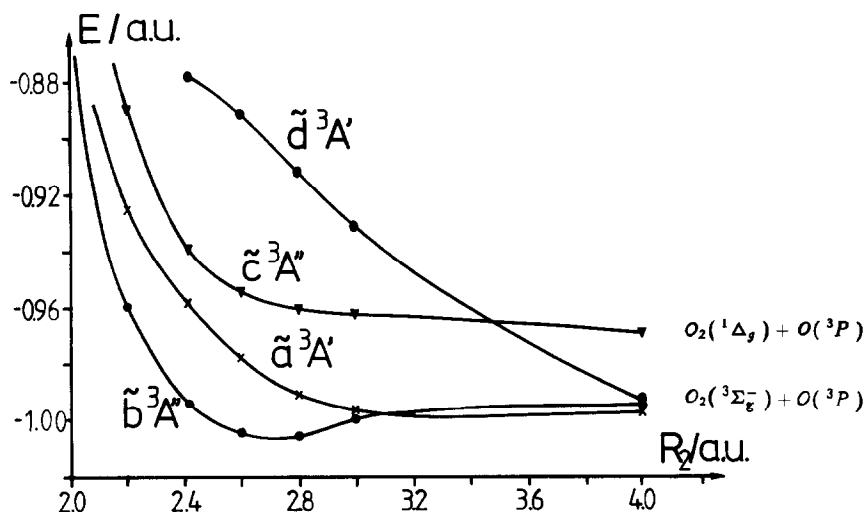


Fig. 12. Calculated potential energy curves for the lowest-lying triplet states of ozone as a function of R_2 whereby $R_1=2.413 a_0$ and $\gamma=100^\circ$. The estimated full-CI energy is given as $E_{\text{FCI}} = -224.0 + E$ in a.u.

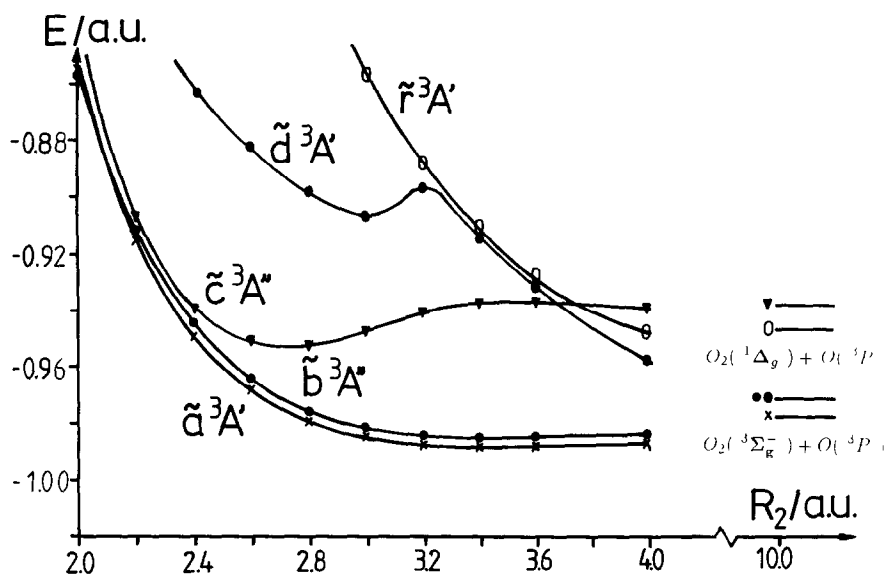


Fig. 13. Calculated potential energy curves for the lowest-lying triplet states of ozone as function of R_2 whereby $R_1 = 2.413 a_0$ and $\gamma = 116.8^\circ$. The estimated full-CI energy is given as $E_{\text{FCI}} = -224.0 + E$ in au.

Table 13

Character of triplet electronic states. Given are the occupation numbers for the molecular orbitals in the dominant configurations at various internuclear separations R_2 for fixed geometry values ($R_1 = 2.413 a_0$; $\gamma = 116.8^\circ$), and the weight K of all reference configurations ($K = \sum \text{ref } c_i^2$) in the CI expansion

| State | $R_2 = 2.413 a_0$ orbitals ^{a)} | | | | | | | | $R_2 = 3.00 a_0$ orbitals ^{a)} | | | | | | | | $R_2 = 4.00 a_0$ orbitals ^{a)} | | | | | | | |
|------------------|---|-----|------|------|------|------|------|------|--|-----|------|------|------|------|------|------|--|-----|------|------|------|------|------|------|
| | 8a' | 9a' | 10a' | 11a' | 1a'' | 2a'' | 3a'' | K | 8a' | 9a' | 10a' | 11a' | 1a'' | 2a'' | 3a'' | K | 8a' | 9a' | 10a' | 11a' | 1a'' | 2a'' | 3a'' | K |
| \tilde{a}^3A' | 2 | 2 | 2 | 0 | 2 | 1 | 1 | 0.91 | 2 | 2 | 2 | 0 | 2 | 1 | 1 | 0.92 | 2 | 2 | 2 | 0 | 2 | 1 | 1 | 0.92 |
| | - | - | - | - | - | - | - | | 2 | 2 | 2 | 0 | 1 | 1 | 2 | | - | - | - | - | - | - | - | |
| | - | - | - | - | - | - | - | | 2 | 2 | 1 | 1 | 2 | 1 | 1 | | 2 | 2 | 1 | 1 | 2 | 1 | 1 | b) |
| \tilde{b}^3A'' | 2 | 1 | 2 | 0 | 2 | 1 | 2 | 0.90 | 2 | 1 | 2 | 0 | 2 | 1 | 2 | 0.91 | - | - | - | - | - | - | - | 0.92 |
| | 2 | 1 | 2 | 0 | 2 | 2 | 1 | | 2 | 1 | 2 | 0 | 2 | 2 | 1 | | 2 | 1 | 2 | 0 | 2 | 2 | 1 | |
| | - | - | - | - | - | - | - | | - | - | - | - | - | - | - | | 1 | 1 | 1 | 2 | 1 | 2 | 2 | |
| \tilde{c}^3A'' | 2 | 2 | 1 | 0 | 2 | 2 | 1 | 0.90 | 2 | 2 | 1 | 0 | 2 | 2 | 1 | 0.91 | - | - | - | - | - | - | - | 0.92 |
| | - | - | - | - | - | - | - | | 2 | 2 | 0 | 1 | 2 | 2 | 1 | | - | - | - | - | - | - | - | |
| | - | - | - | - | - | - | - | | - | - | - | - | - | - | - | | 1 | 1 | 1 | 2 | 1 | 2 | 2 | |
| \tilde{d}^3A' | 2 | 1 | 1 | 0 | 2 | 2 | 2 | 0.90 | 2 | 1 | 1 | 0 | 2 | 2 | 2 | 0.91 | - | - | - | - | - | - | - | 0.92 |
| | - | - | - | - | - | - | - | | 1 | 1 | 1 | 1 | 2 | 2 | 2 | | - | - | - | - | - | - | - | |
| | - | - | - | - | - | - | - | | - | - | - | - | - | - | - | | 2 | 1 | 2 | 1 | 2 | 1 | 1 | d) |

^{a)} See characterization in a) of table 4.

^{b)} See description of the configuration in footnote b) of table 4.

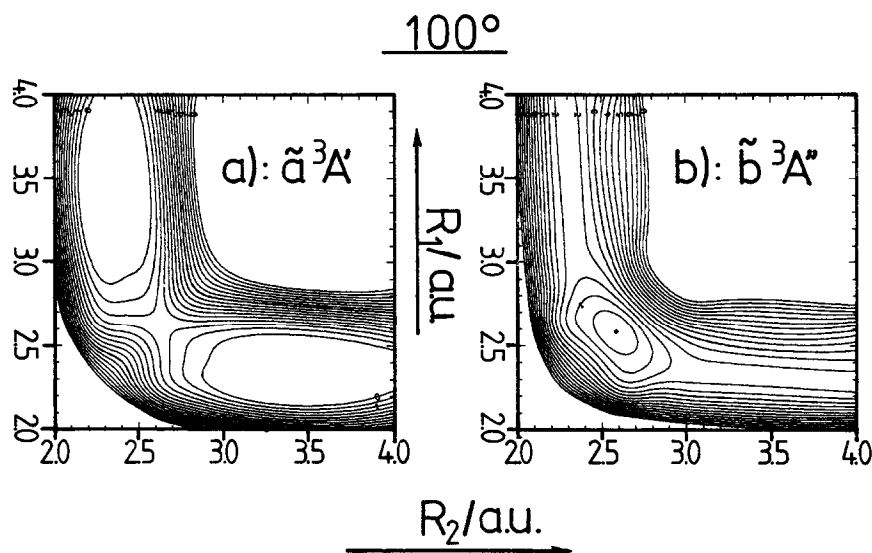
^{c)} See description of the configuration in footnote c) of table 4.

^{d)} See description of the configuration in footnote d) of table 4.

Table 14

Calculated spectroscopic parameters for the triplet states of O₃ (distances in *a*₀ and energies in eV)

| Electronic states in | | Excitation energy | | Optimized equilibrium geometry (<i>R</i> ₁ , <i>R</i> ₂ , <i>γ</i>) present work | Barriers and dissociation energy | | Expected nature from the present results |
|-------------------------------|--|-------------------|-----------|--|-----------------------------------|-----------------------------------|--|
| C _{2v} | C _s | vertical | adiabatic | | theory ₁ ^{a)} | theory ₂ ^{b)} | |
| 1 ³ B ₂ | \tilde{a}^3A' | 1.67 | – | – ^{c)} | – | – | unbound |
| 1 ³ A ₂ | { \tilde{b}^3A'' \tilde{c}^3A'' } | 1.73 | ≈ 0.90 | (2.57, 2.57, ≈ 100°) | –0.25 | 0.19 | bound |
| 1 ³ B ₁ | | 1.91 | 1.49 | (2.55, 2.55, –) ^{c)} | –0.23 | > 0.22 | bound |
| 2 ³ B ₂ | \tilde{d}^3A' | 4.00 | 3.25 | (2.60, 2.60, –) ^{c)} | ≈ 0.20 | – | bound |

^{a)} See note b) in table 5; only the \tilde{a}^3A' possesses a barrier.^{b)} See note c) in table 5.^{c)} For these states the angle has not been optimized and a lower adiabatic energy can be expected. In case of the \tilde{a}^3A' state a weakly bound state can be expected in the 100°–116° angle range [46].Fig. 14. Contour plots of the calculated two-dimensional (*R*₁, *R*₂) PES at *γ* = 100° for the states: (a) \tilde{a}^3A' and (b) \tilde{b}^3A'' . The difference in contour lines is 1000 cm^{–1} (≈ 0.124 eV).

and 1³B₁ in C_{2v} symmetry it is known that these states cross at larger internuclear separation in the neighborhood of *R*₁ = *R*₂ = 2.85 *a*₀ for *γ* = 100° [46]. In the CI description the wavefunction of the \tilde{b}^3A'' state is between *R*₂ = 2.0 *a*₀ and *R*₂ ≤ 3.2 *a*₀ (for *R*₁ = 2.413 *a*₀ and *γ* = 100.0°) dominated by the configuration $\hat{J} = \dots 8a'^2 9a'^1 10a'^1 1a''^2 2a''^2 3a''^1$ (one-electron excitation). At higher angle values (*R*₁ = 2.413 *a*₀ and *γ* = 116.8°, see table 13) the configurations $\hat{K} = \dots 8a'^2 9a'^1 10a'^2 1a''^2 2a''^2 3a''^1$ (one-electron excitation) and $\hat{M} = \dots 8a'^2 9a'^1 10a'^2 1a''^2 2a''^1 3a''^2$ (two-electron

excitation) are predominant in the wavefunction between *R*₂ = 2.0 *a*₀ and 3.2 *a*₀. For *R*₂ > 3.2 *a*₀ in case of both angle values the four-open-shell configuration $\hat{L} = \dots 8a'^2 9a'^1 10a'^1 11a'^1 1a''^2 2a''^2 3a''^1$ is the leading term in the wavefunction describing at the dissociation limit the same fragmentation as in case of the \tilde{A}^1A'' state. Based on the present CI description it is expected that the interaction between both ³A'' states leads to a potential barrier for the lower state which can be found for angle values lower than *γ* = 116.8° and higher than 100°.

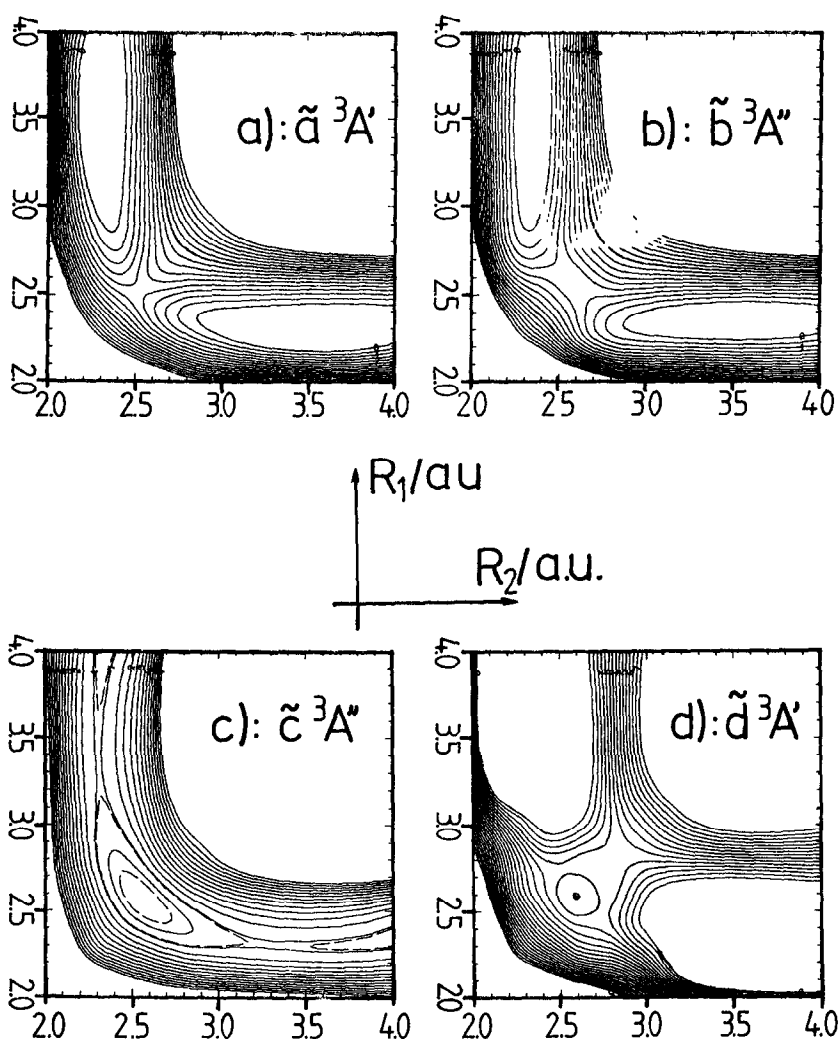


Fig. 15. Contour plots of the calculated two-dimensional (R_1, R_2) PES at $\gamma=116.8^\circ$ for: (a) \tilde{a}^3A' , (b) \tilde{b}^3A'' , (c) \tilde{c}^3A'' and (d) \tilde{d}^3A' . The difference in contour lines is 1000 cm^{-1} ($\approx 0.124\text{ eV}$).

(iii) The excited state \tilde{c}^3A'' which fragments into $O(^3P_g) + O_2(a^1A_g)$ has been calculated with a vertical energy of 1.91 eV and with an adiabatic energy of 1.49 eV. As shown in figs. 13 and 15c this state is well bound with an equilibrium geometry of $R_1 = R_2 = 2.55 a_0$. No potential barrier has been found towards dissociation. The calculated dissociation energy of 0.22 eV has been estimated without angle optimization and should therefore be the lower limit. Ab initio calculations for the symmetric arrangement predict an equilibrium angle of about 121° – 124° [15,33,46].

Between $R_2 = 2.0 a_0$ and $3.2 a_0$ the wavefunction is

described in the main by the configuration \hat{J} . For $R_2 > 3.2 a_0$ the four-open-shell configuration \hat{L} is the leading term in the wavefunction and it describes at $R_2 = 10.0 a_0$ the dissociation limit $^3P_g(\dots 2p_x^2 2p_y^1 2p_z^1) + a^1\Delta_g(\dots 1\pi_{ux}^2 1\pi_{uy}^2 1\pi_{gx}^1 1\pi_{gy}^1)$.

(iv) The excited state \tilde{d}^3A' which dissociates in the lowest fragmentation channel $O(^3P_g) + O_2(X^3\Sigma_g^-)$, has a vertical energy of 4.0 eV. As shown in figs. 12, 13 and 15d (for $\gamma = 116.8^\circ$) it possesses a small barrier which separates the global minimum (calculated at $R_1 = R_2 = 2.60 a_0$ and with an adiabatic energy of 3.25 eV) from the dissociation limit. The

calculated energy difference from minimum to the top of the barrier is about 0.20 eV. Generally, this state shows a similar behavior for the PES as the \tilde{C}^1A' state (see table 5 and fig. 4c). At $\gamma=100^\circ$ the \tilde{d}^3A' state shows repulsive behavior.

The wavefunction of this state for $\gamma=116.8^\circ$ and $R_1=2.413 a_0$ is dominated between $R_2=2.0 a_0$ and $3.2 a_0$ by the two-open-shell configuration $\hat{D}=\dots 8a'^1 10a'^1 1a''^2 2a''^2 3a''^2$ (two-electron excitation) as in case of the \tilde{C}^1A' state. For $R_2>3.2 a_0$ the configuration $\hat{F}=\dots 8a'^2 9a'^1 10a'^2 11a'^1 1a''^2 2a''^1 3a''^1$ describes the fragmentation in a similar way as in case of the \tilde{C}^1A' state.

6. Discussion and interpretation of the results

The lowest observed absorption band in ozone is the 1.2 eV ($\lambda \approx 1050$ nm) band. It has tentatively been assigned as the forbidden \tilde{a}^3A' (1^3B_2) $\leftarrow X^1A'$ transition [54]. This band is about 30 times weaker ($\sigma \approx 2.56 \times 10^{-24}$ cm²) than the stronger vibrational components of the Wulf band [663–1000 nm]. Anderson et al. [16] discussed the possibility that this band can be modelled as a vibronically allowed $1^1A_2(001) \leftarrow X^1A_1(000)$ transition.

Based on the present results this band could also be interpreted as a hot band of the vibronically induced $\tilde{A}^1A''(1^1A_2) \leftarrow X^1A'$ transition with $(010)' \leftarrow (001)''$ and $(001)' \leftarrow (020)''$. The calculated values for the intensity predict that this band should be about 27 times weaker than the cold band (zero-point energy $E_{001}=1.38$ eV). Such assignment is based on the reasoning that if the transition $\nu'_3=1 \leftarrow \nu''_3=0$ is vibronically allowed, the transition $\nu'_3=0 \leftarrow \nu''_3=1$ should also be possible in the near-infrared spectra. The theoretically simulated band positions for the cold bands can be attributed to the progression $(\nu_1, \nu_2, 1)' \leftarrow (000)''$ for $\nu_1=0, 1, 2$ and $\nu_2=0-6$. In agreement with experiment the intensity of the lines increases with photoexcitation energy. A comparison between normalized experimental absorption cross sections and corresponding theoretical data listed in table 15 shows that the intensity calculated in the purely ab initio treatment at $\lambda=855$ nm is about four times weaker than in measurements. It would certainly be very helpful if detailed experimental knowledge of the temperature dependence of the

photoexcitation bands for $\lambda \geq 700$ nm would be available in order to check the present interpretation of this portion of the Wulf band system.

In the Franck–Condon region ($\gamma=116.8^\circ$) the \tilde{A}^1A'' just discussed shows a repulsive behavior and the transition moments (table 9) are stronger than at the \tilde{A} equilibrium angle value $\gamma=100^\circ$. In previous work [44] the absorption spectrum for this transition has been modelled in a very simple manner. This simulation of the $^1A'' \leftarrow X^1A'$ transition describes the bell-shaped continuum of the Chappuis band quite well. Connecting the present results to this simulation, the Wulf absorption band (see fig. 1) is interpreted as the “falloff” region to the red side of the Chappuis continuum on which vibrational progressions are superimposed, in a similar manner as the experimental interpretation of the absorption band for the Huggins–Hartley ensemble [10,22,55]. Because the vibrational levels of the \tilde{A}^1A'' are positioned above the dissociation limit, but are separated from the dissociation continuum by a potential barrier (see fig. 8b), this state can predissociate by tunneling. Experimental observations [12,16] report that the progressions increase rapidly in width with photoexcitation energy corresponding to lifetimes of $\tau \leq 1 \times 10^{-13}$ s. Other possible radiationless processes which can participate in the predissociation of the \tilde{A} state are intersystem crossings of the \tilde{A} state with the repulsive triplet states \tilde{a}^3A' and \tilde{b}^3A'' (see figs. 8b, 12 and 13).

On the blue side of the bell-shaped continuum in the Chappuis absorption band the fine structure can be interpreted as series of vibrational transitions coming from the transition $\tilde{B}^1A'' \leftarrow X^1A'$ superimposed on the continuum ($\tilde{A}^1A'' \leftarrow X^1A'$) in the “falloff” region. The simulated band line positions show a very good agreement with the experiment. Since the \tilde{B} state is found to be a well-bound state and no evidence for spontaneous emission ($\lambda=410-660$ nm) has been observed so far, it can be speculated that the \tilde{B} state predissociates via nonadiabatic couplings (conical intersections) with the \tilde{A} state (see figs. 8a and 8b). An indirect confirmation for this assumption has recently been reported experimentally [14]. The results show that the time constant for internal conversion from the 1^1B_1 to the 1^1A_2 state following excitation in the $\lambda=624$ nm range is about 90 fs, leading to dissociation into the O+O₂ ground state

Table 15

Comparison of theoretical estimated absorption cross sections with experiment

| Wavelength range (nm) | $\sigma_{\text{exp}}^{\text{a)}}$ | $\sigma_{\text{theo}}^{\text{b)}}$ | Assigned transition to |
|-----------------------|-----------------------------------|------------------------------------|--------------------------------|
| 183.5–185.2 | 0.21 | 0.33 | $\tilde{\text{R}}$ |
| 224.7–227.3 | 1 | 1 | $\tilde{\text{D}}$ |
| 281.7–286.0 | 0.83 | 0.46 | $\tilde{\text{D}}$ |
| | | 0.10×10^{-4} | $\tilde{\text{C}}$ |
| 342.5–347.5 | 0.52×10^{-4} | 0.03 | $\tilde{\text{D}}$ |
| | | $2.0\text{--}4.0 \times 10^{-6}$ | $\tilde{\text{C}}$ |
| 472.5–477.5 | 0.15×10^{-3} | 0.06×10^{-3} | $\tilde{\text{B}}$ |
| 847.5–852.5 | 0.45×10^{-4} | 0.12×10^{-4} | $\tilde{\text{A}}^{\text{c)}}$ |

^{a)} The values are normalized to the value of the Hartley absorption band $\sigma(227 \text{ nm}) = 3.24 \times 10^{-18} \text{ cm}^2$. The values are from ref. [3] measured at $T = 203 \text{ K}$.

^{b)} The values are normalized to the calculated value for the transition $\tilde{\text{D}}^1\text{A}' \leftarrow \text{X}^1\text{A}'$ at 227 nm.

^{c)} In this case the vibrational transition to the local minimum of the excited state for the respective photoexcitation energy range is considered.

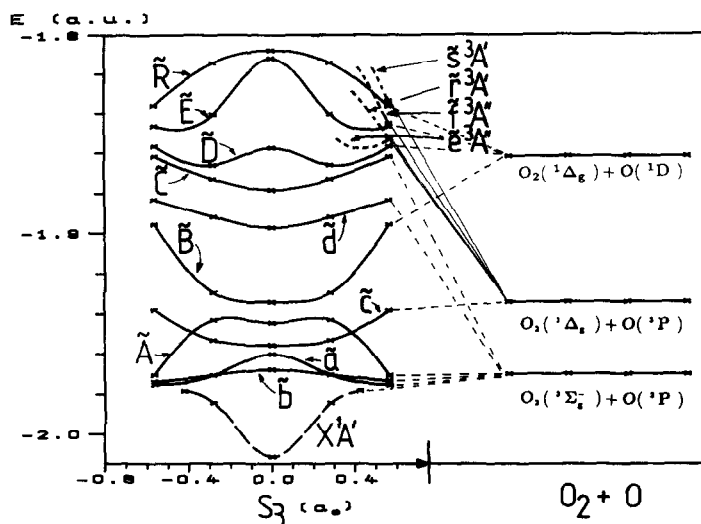


Fig. 16. Calculated potential curves for the singlet and triplet excited states in ozone as function of the C_{2v} internal coordinate s_3 at $s_1 = 3.677 a_0$ and $s_2 = \gamma = 116.8^\circ$. Their correlation to the fragmentation limit $\text{O} + \text{O}_2$ is also shown schematically. The ground state given by the broken line is shown for $s_1 = 3.390 a_0$ and $\gamma = 116.8^\circ$ (equilibrium geometry) as a function of s_3 . The estimated full-CI energy is given as $E_{\text{FCI}} = -223.0 + E$ in au.

fragments. As shown in fig. 16, for higher photoexcitation energies a crossing between the PES of the $\tilde{\text{B}}^1\text{A}'$ state and the triplet state $\tilde{\text{d}}^3\text{A}'$ exists influencing the fragmentation. The interaction between $\tilde{\text{B}}$ and the triplet states due to spin–orbit coupling could also perturb the high-lying vibrational levels of the $\tilde{\text{B}}$ state

suggesting a predissociative nature in the absorption band.

Measurements in the range $T = -78$ to 90°C [9,10,23,56] have shown that an important temperature dependence exists for the lowest part of the Huggins band ($\lambda = 336\text{--}361 \text{ nm}$). The observed hot-band spectra [9,10,20,21,23,56] show clearly a rela-

tively low-temperature sensitivity of the bands at $\lambda = 343.9$ nm (29082 cm $^{-1}$), 347.2 (28805 cm $^{-1}$) and 351.4 nm (28465 cm $^{-1}$). Based on the present ab initio calculations these lines can be interpreted as the vibrational transitions to $(000)'$ and $(010)'$ of the \tilde{C} state at the energies 28465 and 28805 cm $^{-1}$, respectively, and as the transition to $(000)'$ of the \tilde{D} state at 29082 cm $^{-1}$ the lines of weak intensity are thereby ascribed to vibrational transitions to the \tilde{C} state and the strong ones are interpreted as transitions to the \tilde{D} state. In this general sense the present interpretation agrees with previous interpretations [22,49,55] that the Huggins system partly corresponds to transitions into the bound portions of the \tilde{D}^1A' (1^1B_2) PES with relatively weak Franck-Condon factors. For photoexcitations at $\lambda \leq 300$ nm (above the dissociation limit of $O(^1D_g) + O_2(a^1\Delta_g)$) the bell-shaped continuum (Hartley band) corresponds to transitions into the repulsive potential region of the \tilde{D} surface [57] from the equilibrium geometry of the ground state with strong Franck-Condon overlap. Due to the asymmetric distortion of the \tilde{D} state the component μ_y (see table 8) dominates in the spectrum describing the vibrational transitions to the $v'_3 = 0, 1, \dots$ levels.

There is experimental evidence that the line widths in the Huggins absorption depend on the excitation energy. For excitations between 28000 and 30400 cm $^{-1}$ ($329 \leq \lambda \leq 357$ nm) the decay time of the lower vibrational levels has been calculated as $\tau \approx 2 \times 10^{-13}$ s [21]; at higher excitation energies between 30600 and 31000 cm $^{-1}$ ($323 \leq \lambda \leq 327$ nm) a calculated predissociation lifetime of $\tau \approx 3.6 \times 10^{-12}$ s is reported [22]. As noted previously, the \tilde{C} state is a weakly bound state separated from the dissociation region by a potential barrier. Based on the present PES results, tunneling could possibly be the radiationless process leading to the observed predissociative nature of the vibrational levels. In case of the \tilde{D} state, the observed predissociation could be partly due to the nonadiabatic coupling between this state and the \tilde{C} state leading to $O(^3P_g) + O_2(X^3\Sigma_g^-)$ photofragments.

On the other hand, taking into account the PES of the triplet states, as shown schematically in fig. 16, mixing of the higher-lying \tilde{D}^1A' state with the repulsive portion of triplet states by spin-orbit coupling could also perturb the absorption spectra. Such a pro-

cess has been proposed for the equivalent states in SO_2 [58–60], but in ozone this coupling may lead to fragmentation (photopredissociation). The possible participating triplet states are correlated to the fragmentation channels $O(^3P_g) + O_2(a^1\Delta_g)$, $O(^3P_g) + O_2(b^1\Sigma_g^+)$ and $O(^1D_g) + O_2(X^3\Sigma_g^-)$, which are below the dissociation limit of the \tilde{D} state (at about 32900 cm $^{-1}$). Measurements have reported that the Huggins absorption band is importantly perturbed for $\lambda \leq 313.5$ nm ($E \geq 31900$ cm $^{-1}$) [9,20]. Moreover, the present simulated absorption spectrum of the Huggins band shows for a noncoupled model between the \tilde{C} and \tilde{D} states, that the transitions to \tilde{C} as listed in table 15 are weak, but eventually participate actively in the Huggins band. Brand et al. [21] reported an oscillator strength of roughly $f_e \approx 1.0 \times 10^{-5}$ for this band in the energy range $E = 28400$ – 30500 cm $^{-1}$. This value is consistent with our computations. At higher excitation energies $\lambda \leq 300$ it is expected that both states \tilde{C} and \tilde{D} can absorb and fragmentate leading to the production of 3P_g and 1D_g atoms, respectively; for $\lambda \leq 300$ nm both states are placed above the fragmentation limit $O(^1D_g) + O_2(a^1\Delta_g)$.

In considering ozone fragmentation it is important to realize that the dissociation channel leading to three oxygen atoms $O(^3P_g)$ is also at relatively low energy (≈ 6.24 eV), compared to the various $O_2 + O$ channels listed in table 16. The number of states actually considered in the present work is also shown in this table and the comparison between the experimental and calculated data indicate the numerical accuracy of the present calculations. From the modelling view it is the third dissociation mechanism, if the symmetric removal of the central atom ($O + O_2$) as discussed earlier [40,46] and the asymmetric bond breaking as treated in the present work are considered to be the other two.

Fig. 17 presents schematically the fragmentation path for the ground state X^1A' and the excited states \tilde{D}^1A' and \tilde{R}^1A' for which the strongest transition moments (tables 8 and 9) have been found. The fragmentation of these states into $O + O_2$ is described for $R_2 \rightarrow \infty$ at fixed values for R_1 and γ ; the fragmentation into $3 \times O(^3P_g)$ is described for $R_1 = R_2 = R$ elongation at fixed γ value parting from the Franck-Condon region.

As discussed earlier, the \tilde{R}^1A' state correlates with

Table 16

Comparison between experimental and calculated dissociation limits of ozone as obtained from the optimized geometry: R_1 = optimum, $R_2 = 10.00 a_0$ and $\gamma = 116.8^\circ$; the values are averaged over the total number of states calculated for the supermolecule in the respective dissociation channel. States of quintet multiplicity have been considered for $R_1 = 2.60 a_0$. Energies are given in eV

| O ₂ + O | Exp. | Present | States in O ₃ (C _s) | | | | | | TNS/NS ^{a)} |
|--|-------------------|-------------------|--|------------------|-----------------|------------------|-----------------|------------------|----------------------|
| | | | ¹ A' | ¹ A'' | ³ A' | ³ A'' | ⁵ A' | ⁵ A'' | |
| X ³ Σ _g ⁻ + ³ P _g | 0.0 ^{b)} | 0.0 ^{c)} | 2 | 1 | 2 | 1 | 2 | 1 | 9/9 |
| a ¹ Δ _g + ³ P _g | 0.978 | 1.042 | – | – | 3 | 3 | – | – | 6/6 |
| b ¹ Σ _g ⁺ + ³ P _g | 1.630 | 1.784 | – | – | 1 | 2 | – | – | 3/3 |
| X ³ Σ _g ⁻ + ¹ D _g | 1.970 | 2.165 | – | – | 2 | 3 | – | – | 5/3 |
| a ¹ Δ _g + ¹ D _g | 2.950 | 3.062 | 5 | 5 | – | – | – | – | 10/4 |
| b ¹ Σ _g ⁺ + ¹ D _g | 3.600 | – | 3 | 2 | – | – | – | – | 5/– |
| c ¹ Σ _u ⁻ + ³ P _g | 4.050 | – | – | – | 2 | 1 | – | – | 3/– |
| X ³ Σ _g ⁻ + ¹ S _g | 4.180 | – | – | – | – | 1 | – | – | 1/– |
| A ³ Δ _u + ³ P _g ^{d)} | 4.260 | 4.33 | 3 | 3 | 3 | 3 | 3 | 3 | 18/6 |
| A ³ Σ _u ⁺ + ³ P _g ^{d)} | 4.340 | 4.59 | 1 | 2 | 1 | 2 | 1 | 2 | 9/2 |
| a ¹ Δ _g + ¹ S _g | 5.160 | – | 1 | 1 | – | – | – | – | 2/– |
| 3 × ³ P _g ^{e,f)} | 6.240 | – | 13 | 14 | 13 | 14 | 13 | 14 | 81/– |
| b ¹ Σ _g ⁺ + ¹ S _g | 6.850 | – | 1 | – | – | – | – | – | 1/– |
| c ¹ Σ _u ⁻ + ¹ D _g | 7.090 | – | 2 | 3 | – | – | – | – | 5/– |

^{a)} TNS: total number of states for the channel; NS: number of states considered in the calculations.

^{b)} The zero of energy is chosen to be the experimental dissociation energy value $D_e = 1.13$ eV [24]. For each electronic state of the diatomic fragment the energy difference between the 0–0 vibrational levels of the respective states has been considered.

^{c)} The theoretical zero of energy is the estimated full CI energy $E_0 = -224.97363$ hartree, averaged over all electronic states which dissociate into the lowest fragmentation channel X ³Σ_g⁻ + ³P_g.

^{d)} Only the quintet electronic states have been considered.

^{e)} This fragmentation channel is given for the set of coordinates: γ fixed and $R_1 = R_2 = R \geq 5.00 a_0$ or $R_2 \geq 5.00 a_0$ and $R_1 \geq R_2$.

^{f)} Also electronic states with higher multiplicity ⁷A' (13) and ⁷A'' (14) exist for this dissociation channel; in C_{2v} symmetry the states considered are correlated with ^{1,3,5,7}(6A₁ + 7B₁ + 7B₂ + 7A₂).

the 2 ¹B₂ for vertical excitations. It shows repulsive behavior (see figs. 4a–4c and 16) towards the fragmentation channel O(¹D_g) + O₂(a ¹Δ_g) for the asymmetric dissociation pathway. Moreover, it is placed above the fragmentation limit 3 × O(³P_g), i.e. this state possesses three pathways for dissociation from which the fragmentation can be accompanied by the production of O(³P_g) and O(¹D_g) atoms. As shown in table 15 the expected theoretical value for the absorption cross section at $\lambda = 183.2$ – 185.2 nm described by the transition $\tilde{R}^1A' \leftarrow X^1A'$ (denoted here as the R-band) is in good agreement with measured data. Photodynamical calculations [57] find a bell-shaped continuum for $\lambda = [220$ – $180]$ nm due to the favorable Franck–Condon overlap. The calculated absorption window between this band and the Hartley bell-shaped continuum is obtained around $\lambda \approx 217$ nm (exp. 200.0–204 nm [3]). Experimental quantum yield measurements for the formation of O(¹D_g) and

O(³P_g) from photolysis of ozone at $\lambda \leq 193$ nm [61,62] find a net production of odd oxygen atoms of about 57% at $\lambda \approx 193$ nm and about 135% at $\lambda \approx 157$ nm. They represent an important production compared to the 12% obtained for photoexcitations in the Hartley absorption band at $\lambda = 266$ nm.

In case of the triplet states, the present ab initio results show that the low-lying excited states \tilde{a}^3A' , \tilde{b}^3A'' , \tilde{c}^3A'' and \tilde{d}^3A' are expected to be weakly bound. The \tilde{c}^3A'' state correlates with the fragmentation channel O(³P_g) + O₂(a ¹Δ_g) and the others to the O + O₂ ground state fragments (see figs. 3, 12 and 13). The high-lying states \tilde{e}^3A'' , \tilde{f}^3A'' and \tilde{r}^3A' which are correlated to O(³P_g) + O₂(a ¹Δ_g), are expected to be repulsive. As shown in fig. 16, crossing occurs between the PES of the \tilde{c}^3A'' and the singlet state \tilde{A}^1A'' . In analogy to the case of the \tilde{B}^1A'' and \tilde{D}^1A' states, it may be speculated that predissociation of the \tilde{c}^3A'' state is possible due to spin–orbit coupling making

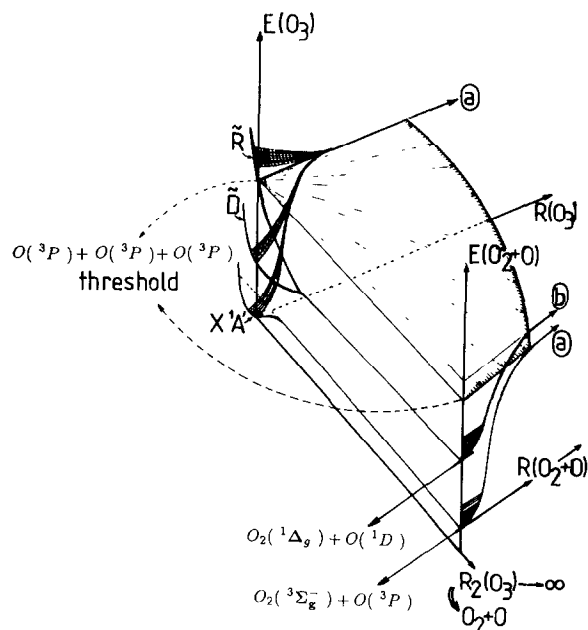
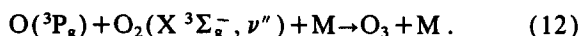
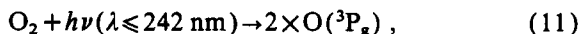


Fig. 17. Schematic picture for the correlation of the ground state X^1A' and the excited D^1A' and R^1A' states with the dissociation limit $O+O_2$ for R_2 elongation at fixed values for R_1 and γ and the dissociation limit $3 \times O(^3P_g)$ for $R_1=R_2=R$ elongation (denoted by (a)), parting from the Franck–Condon region. The fragmentation channel $2 \times O(^3P_g) + O(^1D_g)$ is denoted as (b).

intersystem-crossing and internal-conversion processes possible.

7. Possible atmospheric implications of the excited O_3 states

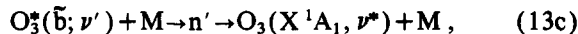
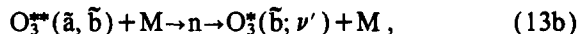
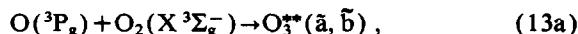
The formation of ozone is generally described by photodissociation of O_2 followed by a recombination process



Reaction (12) is a high-pressure process, which produces ozone in its ground state X^1A' [63,64] and in some low-lying excited triplet electronic states [65,66]. Likewise ozone decomposes into $O+O_2$ upon light absorption as listed in eqs. (1)–(3). Hence there is a subtle balance in the reactions between oxygen atoms, oxygen molecules and ozone, all of them

in a variety of electronic states. Some aspects, based on the present ab initio calculations, can most conveniently be discussed by considering the potential energy surfaces indicated schematically in figs. 16 and 17. The first figure shows the behavior of the important singlet and triplet states of ozone, the second connects the pertinent ozone singlet states with the potential surfaces of the O_2 molecule in its ground $X^3\Sigma_g^-$ and the long-lived $a^1\Delta_g$ state.

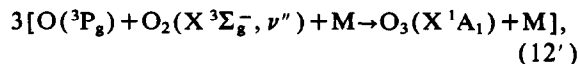
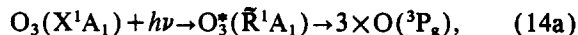
In the collision process eq. (12) involving ground state fragments possible triplet states are \tilde{a}^3A' and \tilde{b}^3A'' (fig. 16). The \tilde{a}^3A' is metastable or repulsive, the \tilde{b}^3A'' is a state with various bound vibrational levels. Interaction with the X^1A' state is also possible by energy transfer processes from \tilde{b}^3A'' state to the O_3 ground state leading to high vibrational ground state levels. This can be summarized by the following chain of reactions:

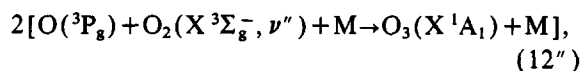
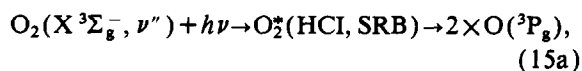


where n and n' define sequences for collisional relaxation.

Production of oxygen atoms occurs either from photolysis of O_2 or O_3 , whereby the ensuing fragments depend on the wavelength of the incident radiation. Fragmentation of oxygen takes place in the atmosphere in several regions. Particularly, in the Schumann Runge bands (SRB) at 175–200 nm photopredissociation processes are present, and in case of the Herzberg continua at 190–242 nm photodissociation processes exist making the Herzberg I continuum (HCI) $A^3\Sigma_u^- \leftarrow (X^3\Sigma_g^-; \nu''=0)$ the primary source of oxygen atoms [67–70].

Based on the present interpretation of the ab initio results, it can be expected that for $\lambda \leq 200$ nm a possible competition occurs between production of odd atoms resulting from absorbing ozone and the previously cited absorption bands of O_2 . This is summarized by the following chain of reactions:





Photoexcitation of ozone into $\tilde{\text{R}}^1\text{A}'$ can lead to three odd atoms which by participating in recombination processes with O_2 produce ozone.

8. Summary and conclusion

The present work has employed large-scale *ab initio* MRD-CI calculations to investigate the potential energy surfaces of the ozone molecule in its ground and eight low-lying excited states, in particular from the equilibrium O_3 geometry to the $\text{O}_2 + \text{O}$ dissociation limit. Spectroscopic parameters are determined for the various states and transition moments from the $\text{X } ^1\text{A}'$ ground state to the excited singlets are calculated.

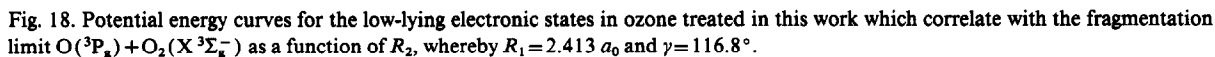
It is found that ozone has a number of singlet and triplet electronic states which are weakly bound ($D_e \leq 0.5$ eV) towards $\text{O}_2 + \text{O}$ dissociation. Two states possess a relatively deep minimum: the $\text{X } ^1\text{A}'$ ground state with the dissociation limit $\text{O}_2(\text{X } ^3\Sigma_g^-) + \text{O}(^3\text{P}_g)$ and the $\tilde{\text{B}}^1\text{A}''$ state with the $\text{O}(^1\text{D}_g) + \text{O}_2(\text{a } ^1\Delta_g)$ dissociation limit. Most of the states which correlate with the lowest fragmentation limit are repulsive or possess only local minima (fig. 18), separated from the dissociation channel by a barrier ($\tilde{\text{A}}$, $\tilde{\text{d}}$, $\tilde{\text{C}}$ states). The three quintet states are entirely repulsive [45]; the $\tilde{\text{b}}$ state is bound with a minimum around $\gamma = 100^\circ$ and the $\tilde{\text{a}}$ state is probably weakly bound with a potential well in the area between $\gamma = 100^\circ$ and $\gamma = 116^\circ$. The absence of fluorescence and phosphorescence processes confirms this general potential surface behavior. In the isovalent SO_2 molecule such processes have been observed at different photoexcitation energies [24,59]. The excited states $\tilde{\text{c}}^3\text{A}''$ and $\tilde{\text{D}}^1\text{A}'$ which correlate with the fragmentation channels $\text{O}_2(\text{a } ^1\Delta_g) + \text{O}(^3\text{P}_g)$ and $\text{O}_2(\text{a } ^1\Delta_g) + \text{O}(^1\text{D}_g)$, respectively, are bound, but due to possible coupling with other states (figs. 4a, 16, 17) they will also show a metastable character.

The simulation of the ozone absorption bands sug-

gests that these can be interpreted in a general form as the ensemble of bands “Wulf–Chappuis” and “Huggins–Hartley” for which the bell-shaped continua can be described as the transitions into the repulsive potential region of the $\tilde{\text{A}}^1\text{A}''$ and $\tilde{\text{D}}^1\text{A}'$ PES, respectively (strong Franck–Condon overlap). The discrete structure for the Wulf and Chappuis absorption bands can result from transitions to the $\tilde{\text{A}}$ state (with relatively weak Franck–Condon factors) and to the $\tilde{\text{B}}$ state, respectively. In case of the Huggins band the calculations suggest that two states participate in the absorption; one describes the discrete structure with weak intensity (transition to $\tilde{\text{C}}$). The other state describes the structure up to the dissociation limit (transition to $\tilde{\text{D}}$) in agreement with previously proposed models for this band.

Experimental investigation of the energy partitioning in the photofragment distribution of $\text{O}_2 + \text{O}$ and the study of the vibrational–rotational spectra of the diatomic fragments produced after photolysis of O_3 at wavelengths between 320 and 295 nm would be of great help to confirm whether the formally spin-forbidden dissociation pathways $\text{O}_3 + h\nu \rightarrow \text{O}_3(\tilde{\text{D}}) \rightarrow \text{O}(^3\text{P}_g) + \text{O}_2(\text{a } ^1\Delta_g)$, $\text{O}(^3\text{P}_g) + \text{O}_2(\text{b } ^1\Sigma_g^+)$ and $\text{O}(^1\text{D}_g) + \text{O}_2(\text{X } ^3\Sigma_g^-)$ play indeed only a minor role in the photochemistry of ozone, as has been assumed so far. Interactions with various triplet species seem possible. At higher photoexcitation energies ($\lambda \leq 295$ nm) both states, $\tilde{\text{C}}$ and $\tilde{\text{D}}$, are expected to dissociate, leading to the production of $^3\text{P}_g$ and $^1\text{D}_g$ atoms, respectively. At $\lambda \leq 217$ nm the $\tilde{\text{R}}$ state can also participate in the production of $^1\text{D}_g$ atoms by photodissociation processes due to the relatively strong transition moment.

Ozone absorption in the Hartley band ($\lambda \leq 300$ nm) produces oxygen atoms $\text{O}(^3\text{P}_g)$ and $\text{O}(^1\text{D}_g)$ whereby the product yield (see eq. (3)) is generally considered to be independent of the photoexcitation energy. An experimental investigation in the wavelength range 200–280 nm would be very important to confirm whether this constant yield is really true, in particular since various (autocatalytic) processes for ozone formation in this energy range are conceivable if not only the singlet but also the triplet fragmentation channel is considered and if deactivation of $\text{O}_2(\text{a } ^1\Delta_g)$ and $\text{O}(^1\text{D}_g)$ to produce $\text{O}(^3\text{P}_g)$ atoms is also taken into account. Details of the $\tilde{\text{C}}$ and $\tilde{\text{D}}$ states and their interaction play a major role thereby.



Acknowledgement

and to Dipl. Hdl. J. Langohr for financial support given to part of this work. The services and computer time made available by the University of Bonn Computer Center have been essential to the present study and are gratefully acknowledged.

References

- [1] S. Chapman, *Mem. Roy. Meteor. Soc.* 103 (1930) 3.
- [2] H.S. Johnston and G. Whitten, *Pure Appl. Geophys.* 106-108 (1973) 1468.
- [3] Global Ozone Research and Monitoring Project Report No. 16: Atmospheric Ozone, World Meteorological Organization, Geneva (1985).
- [4] W.N. Hartley, *J. Chem. Soc.* 39 (1881) 57, 111.
- [5] W. Huggins and Mrs. Huggins, *Proc. Roy. Soc.* 48 (1890) 216;
A. Fowler and R.J. Strutt, *Proc. Roy. Soc. A* 93 (1917) 577.

- [6] J. Chappuis, *Compt. Rend. Acad. Sci. (Paris)* 91 (1880) 985; 94 (1882) 858; *J. Phys. Par. Ser. 2.2* (1882) 494.
- [7] O.R. Wulf, *Proc. Natl. Acad. Sci.* 16 (1930) 507.
- [8] I. Tanaka, E.C.Y. Inn and K. Watanabe, *J. Phys. Chem.* 21 (1953) 1651;
E.C.Y. Inn and Y. Tanaka, *J. Opt. Soc. Am.* 43 (1953) 870.
- [9] J.W. Simons, R.J. Paur, H.A. Webster III and E.J. Bair, *J. Chem. Phys.* 59 (1973) 1203.
- [10] D.E. Freeman, K. Yoshino, J.R. Esmond and W.H. Parkinson, *Planet Space Sci.* 32 (1984) 239.
- [11] J. Heicklein, in: *Atmospheric chemistry* (Academic Press, New York, 1976).
- [12] S.M. Anderson, J. Morton and K. Mauersberger, *J. Chem. Phys.* 93 (1990) 3826.
- [13] C.R. Lefebvre, *Acad. Sci. (Paris)* 200 (1935) 1743.
- [14] Y. Chen, L. Hunziker, P. Ludowise and M. Morgen, *J. Chem. Phys.* 97 (1992) 2149.
- [15] M. Braunstein and R.T. Pack, *J. Chem. Phys.* 96 (1992) 6378.
- [16] S.M. Anderson, J. Maeder and K. Mauersberger, *J. Chem. Phys.* 94 (1991) 6351.
- [17] H.B. Levene, J.C. Nieh and J.J. Valentini, *J. Chem. Phys.* 87 (1987) 2583.
- [18] J.I. Steinfeld, S.M. Adler Golden and I.M. Gallagher, in: *Critical survey of data on the spectroscopy and kinetics of ozone in the upper atmosphere*, *J. Phys. Chem. Ref. Data* 16 (1987) 911.
- [19] E. Vigroux, *Ann. Phys. (Paris)* 8 (1953) 709.
- [20] D.H. Katayama, *J. Chem. Phys.* 71 (1979) 815.
- [21] J.C.D. Brand, K.J. Cross and A.R. Roy, *Can. J. Phys.* 56 (1978) 327.
- [22] A. Sinha, D. Imre, J.H. Goble and J.L. Kinsey, *J. Chem. Phys.* 84 (1986) 6108.
- [23] O.R. Wulf and E.H. Melvin, *Phys. Rev.* 38 (1931) 330.
- [24] G. Herzberg, in: *Electronic spectra and electronic structure of polyatomic molecules* (Van Nostrand, Princeton, 1966).
- [25] J. Malicet, J. Brion and D. Daumont, *Chem. Phys. Letters* 158 (1989) 293.
- [26] M. Griggs, *J. Chem. Phys.* 49 (1968) 857.
- [27] T. Kinugawa, T. Sato and T. Arikawa, *J. Chem. Phys.* 93 (1990) 3289.
- [28] J.J. Valentini, *Chem. Phys. Letters* 96 (1983) 397;
J.J. Valentini, D.P. Gerrity, D.L. Phillips, J.-C. Nieh and K.D. Tabor, *J. Chem. Phys.* 86 (1987) 6745.
- [29] P.W. Fairchild and E.K.C. Lee, *Chem. Phys. Letters* 60 (1978) 36;
C.E. Fairchild, E.J. Stone and G.M. Lawrence, *J. Chem. Phys.* 69 (1978) 3632.
- [30] R.K. Sparks, L.R. Carlson, K. Shobatake, M.L. Kowalczyk and Y.T. Lee, *J. Chem. Phys.* 72 (1980) 1401.
- [31] J.J. Valentini, D.S. Moore and D.S. Bomse, *Chem. Phys. Letters* 83 (1981) 217;
D.S. Moore, D.S. Bomse and J.J. Valentini, *J. Chem. Phys.* 79 (1983) 1745.
- [32] M. Troler and J.R. Wiesenfeld, *J. Geophys. Res.* 93 (1988) 7119.
- [33] P.J. Hay and T.H. Dunning Jr., *J. Chem. Phys.* 67 (1977) 2290;
P.J. Hay, R. TPack, R.B. Walker and E.J. Heller, *J. Phys. Chem.* 86 (1982) 862.
- [34] J.F. Stanton, R.J. Bartlett, D.H. Magers and W.N. Lipscomb, *Chem. Phys. Letters* 163 (1989) 333;
J.F. Stanton, W.N. Lipscomb, D.H. Magers and R.J. Bartlett, *J. Chem. Phys.* 90 (1989) 1077.
- [35] T.J. Lee, *Chem. Phys. Letters* 169 (1990) 529;
T.J. Lee and G.E. Scuseria, *J. Chem. Phys.* 93 (1990) 489.
- [36] K.A. Peterson, R.C. Mayrhofer, E.L. Silbert III and R.C. Woods, *J. Chem. Phys.* 94 (1991) 414.
- [37] K. Yamashita, K. Morokuma, F. Le Quéré and C. Leforestier, *Chem. Phys. Letters* 191 (1992) 515.
- [38] M. Braunstein, P.J. Hay, R.L. Martin and R.T. Pack, *J. Chem. Phys.* 95 (1991) 8239.
- [39] C.W. Wilson Jr. and D.G. Hopper, *J. Chem. Phys.* 74 (1981) 595;
M.V. Ramakrishna and K.D. Jordan, *Chem. Phys.* 115 (1987) 423.
- [40] S.S. Xantheas, G.J. Atchity, S.T. Elbert and K. Ruedenberg, *J. Chem. Phys.* 94 (1991) 8054.
- [41] R.J. Buenker and S.D. Peyerimhoff, *Theoret. Chim. Acta* 39 (1975) 217;
R.J. Buenker, S.D. Peyerimhoff and W. Butscher, *Mol. Phys.* 35 (1978) 771;
R.J. Buenker and S.D. Peyerimhoff, in: *New horizons of quantum chemistry*, eds. P.O. Löwdin and B. Pullmann (Reidel, Dordrecht, 1983) p. 183.
- [42] T.H. Dunning Jr., *J. Chem. Phys.* 53 (1970) 2823.
- [43] K.H. Thunemann, S.D. Peyerimhoff and R.J. Buenker, *J. Mol. Spectry.* 70 (1978) 432.
- [44] A. Banichevich, S.D. Peyerimhoff and F. Grein, *Chem. Phys. Letters* 173 (1990) 1;
A. Banichevich, S.D. Peyerimhoff, J.A. Beswick and O. Atabek, *J. Chem. Phys.* 96 (1992) 6580.
- [45] A. Banichevich, S.D. Peyerimhoff and F. Grein, *Chem. Phys. Letters* 195 (1992) 459.
- [46] A. Banichevich and S.D. Peyerimhoff, *Chem. Phys.* (1993), in press.
- [47] D.J. McCaa and J.H. Shaw, *J. Mol. Spectry.* 25 (1968) 374.
- [48] A. Barbe, C. Secroun and P. Jouve, *J. Mol. Spectry.* 49 (1974) 171.
- [49] F. Le Quéré and C. Leforestier, *Chem. Phys. Letters* 189 (1992) 537.
- [50] G. Herzberg, in: *Spectra of diatomic molecules* (Van Nostrand, Princeton, 1950).
- [51] T.G. Slinger, *J. Chem. Phys.* 65 (1978) 4779.
- [52] K. Weide and R. Schinke, *J. Chem. Phys.* 90 (1989) 7150;
B. Heumann, K. Weide and R. Schinke, *J. Chem. Phys.* (1993), in press.
- [53] V. Vaida, D.J. Donaldson, S.J. Strickler, L. Stephens and J.W. Birks, *J. Phys. Chem.* 93 (1989) 506.
- [54] P.J. Hay, T.H. Dunning Jr. and W.A. Goddard III, *Chem. Phys. Letters* 23 (1973) 456.
- [55] D.G. Imre, J.L. Kinsey, R.W. Field and D.H. Katayama, *J. Phys. Chem.* 86 (1982) 2564.

- [56] W.H. Eberhardt and W. Shand Jr., *J. Phys. Chem.* 14 (1946) 525.
- [57] A. Banichevich, J.A. Beswick and O. Atabek (1991), unpublished work.
- [58] J.C.D. Brand and K. Srikameswaran, *Chem. Phys. Letters* 15 (1972) 130;
J.C.D. Brand, P.H. Chiu and A.R. Hoy, *J. Mol. Spectry.* 60 (1976) 43.
- [59] H. Okabe, in: *Photochemistry of small molecules* (Wiley, New York, 1976).
- [60] H. Kanamori, J.E. Butler, K. Kawaguchi, C. Yamada and E. Hirota, *J. Phys. Chem.* 83 (1985) 611.
- [61] A.A. Turnipseed, G.L. Vaghjiani, T. Gierczak, J.E. Thompson and A.R. Ravishankara, *J. Phys. Chem.* 95 (1991) 3244.
- [62] M.R. Taherian and T.G. Slinger, *J. Phys. Chem.* 83 (1985) 6246.
- [63] C.J. Hochanadel, J.A. Ghormley and J.W. Boyle, *J. Chem. Phys.* 48 (1968) 2416.
- [64] W.T. Rawlins, G.E. Caledonia, J.J. Gibson and A.T. Stair Jr., *Geophys. Res.* 90 (1985) 2896;
W.T. Rawlins and R.A. Armstrong, *J. Chem. Phys.* 87 (1987) 5202.
- [65] T. Kleindienst, J.R. Locker and E.J. Bair, *J. Photochem.* 12 (1980) 67;
T. Kleindienst, J.B. Burkholder and E.J. Bair, *Chem. Phys. Letters* 70 (1980) 117.
- [66] J.R. Locker, J.A. Jones and E.J. Bair, *J. Photochem.* 36 (1987) 235.
- [67] A.S.C. Cheung, K. Yoshino, W.H. Parkinson, S.L. Gubermann and D.E. Freeman, *Planet. Space Sci.* 34 (1986) 1007.
- [68] M. Nicolet and R. Kennes, *Planet. Space Sci.* 11 (1986) 1043.
- [69] J.W. Meriwether, *J. Geophys. Res.* 94 (1989) 14629.
- [70] M. Allen, *J. Geophys. Res.* 91 (1986) 2844;
M. Allen, J.I. Lunine and Y.L. Yung, *J. Geophys. Res.* 89 (1984) 4841.